Title

Electronically Coupled 2D Polymer/MoS2 Heterostructures



Journal

Journal of the American Chemical Society, 142(50)

ISSN

0002-7863

Authors

Balch, Halleh B

Evans, Austin M

Dasari, Raghunath R

et al.

Publication Date

2020-12-16

DOI

10.1021/jacs.0c10151

Peer reviewed

# Electronically Coupled 2D Polymer / $MoS_2$ Heterostructures

Halleh B. Balch[1,2,3], Austin M. Evans[†4], Raghunath R. Dasari[†5], Hong Li[†5,6], Ruofan Li[†7], Simil Thomas[5,8], Danqing Wang[1,2,3], Ryan P. Bisbey[4,10], Kaitlin Slicker[5], Ioannina Castano[4], Sangni Xun[5], Lili Jiang[1,2,3], Chenhui Zhu[11], Nathan Gianneschi[4,12-17], Daniel C. Ralph[7,9], Jean-Luc Brédas[5,6], Seth R. Marder[5], William R. Dichtel[4], Feng Wang*[1,2,3]

Affiliations:
1 Department of Physics, University of California, Berkeley, CA 94720, USA
2 Kavli Energy Nanosciences Institute, University of California Berkeley, Berkeley, CA 94720, USA
3 Materials Sciences Division, Lawrence Berkeley National Lab, Berkeley, CA 94720, USA
4 Department of Chemistry, Northwestern University, Evanston, IL 60208, USA
5 School of Chemistry and Biochemistry and Center for Organic Photonics and Electronics, Georgia Institute of Technology, Atlanta, GA 30332, USA
6 Department of Chemistry & Biochemistry, University of Arizona, Tucson, AZ 85721, USA
7 Department of Physics, Cornell University, Ithaca, NY 14853, USA
8 Department of Physics, Govt. College Nedumangad, Kerala, 695541, India
9 Kavli Institute at Cornell, Cornell University, Ithaca, NY 14853, USA
10 Department of Chemistry, Cornell University, Ithaca, NY 14853, USA
11 Advanced Light Source, Lawrence Berkeley National Lab, Berkeley, CA 94720, USA
12 Department of Materials Science and Engineering, Northwestern University, Evanston, IL 60208, USA
13 Department of Biomedical Engineering, Northwestern University, Evanston, IL 60208, USA
14 Department of Pharmacology, Northwestern University, Chicago, IL 60611, USA
15 International Institute for Nanotechnology, Northwestern University, Evanston, Illinois 60208, USA
16 Simpson Querrey Institute, Northwestern University, Evanston, Illinois 60208, USA
17 Chemistry of Life Processes Institute, Northwestern University, Evanston, Illinois 60208, USA
† denotes equal contribution
* Corresponding author. Email: fengwang76@berkeley.edu

## Abstract:

**Emergent quantum phenomena in electronically coupled two-dimensional heterostructures are central to next-generation optical, electronic, and quantum information applications. Tailoring electronic band gaps in coupled heterostructures would permit control of such phenomena and is the subject of significant research interest. Two-dimensional polymers (2DPs) offer a compelling route to tailored band structures through the selection of molecular constituents. However, despite the promise of synthetic flexibility and electronic design, fabrication of 2DPs that form electronically coupled 2D heterostructures remains an outstanding challenge. Here, we report the rational design and optimized synthesis of electronically coupled semiconducting 2DP/2D transition metal dichalcogenide van der Waals heterostructures, demonstrate direct exfoliation of the highly crystalline and oriented 2DP films down to a few nanometers, and present the first thickness-dependent study of 2DP/$MoS_2$ heterostructures. Control over the 2DP layers reveals enhancement of the 2DP photoluminescence by two orders of magnitude in ultrathin sheets and an unexpected thickness-dependent modulation of the ultrafast excited state dynamics in the 2DP/$MoS_2$ heterostructure. These results provide fundamental insight into the electronic structure of 2DPs and present a route to tune emergent quantum phenomena in 2DP hybrid van der Waals heterostructures.**

## Introduction

Strong interlayer electronic interactions between two-dimensional materials give rise to quantum phenomena in van der Waals (vdW) heterostructures that are of both fundamental interest and practical importance. For example, vdW heterostructures composed of semiconducting transition metal dichalcogenides (TMDCs) exhibit useful properties such as exceptionally long spin and valley polarization lifetimes,[1,2] ultrafast charge transfer between layers,[3−6] and novel exciton physics in Moiré superlattices.[7,8] Such phenomena emerge in TMDC heterostructures through the strong interlayer coupling of electronic states with similar energies. Consequently, the design of new vdW hetero- structures that permit flexible control over the electronic band structure of constituent layers while maintaining strong electronic coupling at the interface is the subject of substantial research interest.

Two-dimensional polymers (2DPs), of which covalent organic frameworks (COFs) are the most synthetically diverse class, provide a compelling route to band structure design and the development of new vdW heterostructures.[9−12] 2DPs are crystalline lattices formed by covalently linking planar molecular monomers into two-dimensional sheets that stack through interlayer vdW coupling. The 2DP electronic band structure can, in principle, be rationally engineered by careful selection of constituent monomers and polymerization

chemistry.[13,14] With emergent properties of heterostructures intimately tied to the electronic states at the interface, the ability to tune the 2DP band structure in 2DP/TMDC vdW heterostructures would enable the design and realization of novel quantum phenomena across extended length scales with atomic precision.

Despite this promise, major challenges in synthesis, fabrication, and measurement have limited the development of semiconducting 2DP films and 2DP/TMDC heterostructures that exhibit significant interlayer electronic coupling. First, monomers designed for 2DP semiconductors should be conjugated systems with an intrinsically small band gap to promote interlayer coupling among 2DP layers and between the 2DP layer and the inorganic TMDC. Second, the 2DP must form as a highly crystalline vdW-layered film with parallel orientation for efficient interlayer electronic coupling in the heterostructure. Finally, the 2DP layer must be homogeneous across extended length scales to permit systematic optical and electronic transport studies of the heterostructure.

Recent work has demonstrated independent advances in 2DP crystallinity,[15−19] observation of topological band structures,[20−23] and monolayer synthesis.[24,25] Interfacial polymerization at solid−vacuum,[23,26] air−liquid,[25,27] and liquid−liquid[28−30] interfaces is now producing high-quality 2DP films, including those with conjugated polymerization chemistries.[31,32] However, these methods have yet to be accessible to a large number of chemical structures, often produce films that lack long-range order, and can be challenging to manipulate. Direct polymerization of 2DPs on submerged substrates has been extensively studied for a variety of chemical precursors and can permit homogeneous direct deposition, potentially promoting high-quality interfaces and strong interlayer electronic coupling. However, despite significant research effort, the observation and control of interlayer electronic coupling in 2DP and 2DP/TMDC heterostructures remains an outstanding challenge.

Here, we report that rational design and high-quality 2DP growth enables formation of layered 2DP/TMDC vdW heterostructures that exhibit strong interlayer electronic coupling and ultrafast energy transfer at the vdW interface with $MoS_2$ (Figure 1). We show that the high materials quality of these 2DP films permits facile manipulation and direct micromechanical exfoliation of large-area 2DP films down to few nanometers thicknesses. This enables the first thickness-dependent optical characterization of 2DP/$MoS_2$ heterostructures, which reveals enhancement of the 2DP's photoluminescence efficiency by over 2 orders of magnitude in

ultrathin heterostructures. We further observe interlayer electronic coupling in 2DP/$MoS_2$ heterostructures through sub-picosecond energy transfer dynamics between the TMDC and the 2DP in the vdW heterostructure. Surprisingly, we find that the rate of transfer dynamics in the heterostructure can increase by over an order of magnitude with increasing thickness of the 2DP. These results suggest that the interlayer coupling of the 2DP has a profound effect on the evolution of the excited state dynamics in 2DPs and 2DP/TMDC heterostructures.

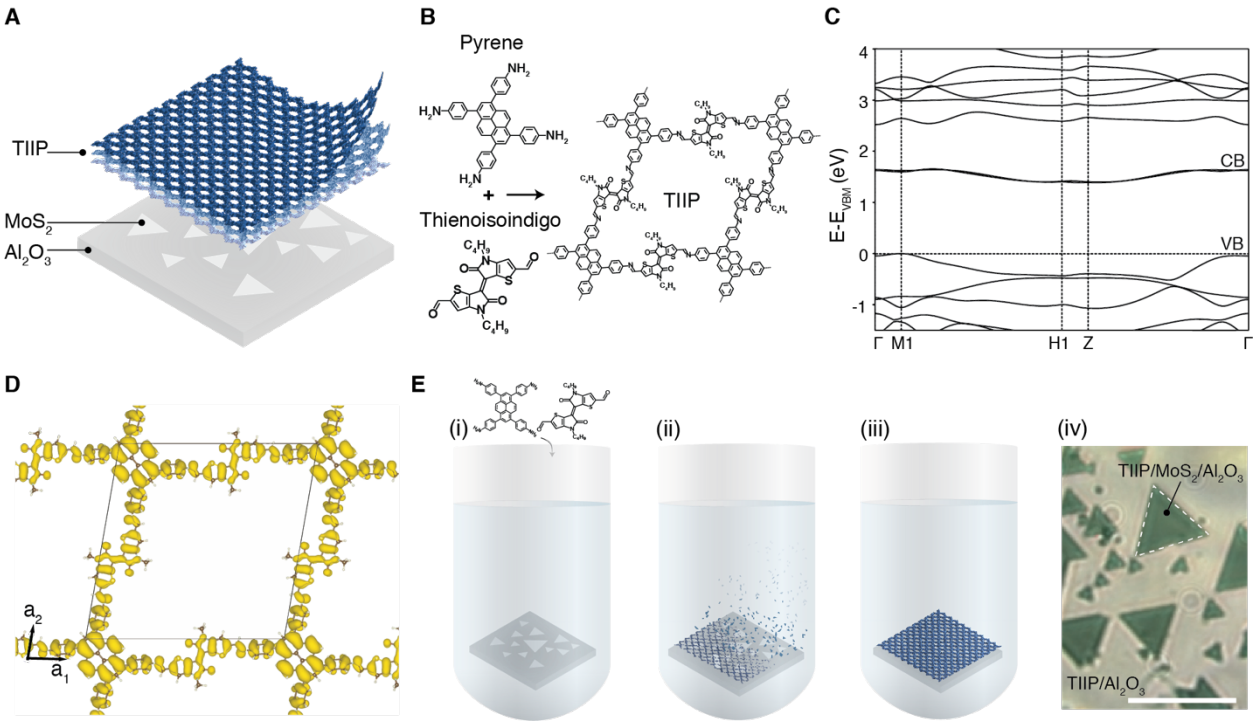


**Figure 1. Design and synthesis of semiconducting 2DP/TMDC heterostructures. (A)** Schematic of the layered TIIP 2DP (blue) on monolayer $MoS_2$ (light grey triangles). $MoS_2$ grown by chemical vapor deposition (CVD) on $Al_2O_3$ (dark grey substrate) appears as triangular single-crystal monolayer flakes (light grey). **(B)** Monomer constituents and TIIP 2DP based on pyrene and thienoisoindigo moieties. **(C)** Electronic band structure of TIIP with a semiconducting bandgap of 1.38 eV along the *M1-H1* direction. **(D)** Electronic structure calculations show that the TIIP valence charge density (yellow) distribution is delocalized across the unit cell. **(E)** Schematic representation of the direct synthesis of 2DP TIIP films on monolayer TMDCs. **(i)** The substrate-supported monolayer TMDC (light grey triangles) on $Al_2O_3$ (dark grey substrate) is submerged in an optimized solvent blend with monomers, **(ii-iii)** substrate-supported direct polymerization of the 2DP forms as a homogeneous, highly crystalline layered film (dark blue), **(iv)** optical micrograph of the resulting TIIP/$MoS_2$ heterostructure shows homogeneous growth of TIIP films across monolayer $MoS_2$. TIIP 2DP grows preferentially on $MoS_2$ flakes seen here in the increased film thickness on the triangular $MoS_2$ flakes. Grey outline identifies one heterostructure of multilayered TIIP/$MoS_2$. Scale bar = 5 $\mu$m.

## Results and Discussion

The bottom-up design of a 2DP semiconductor is challenging because selecting constituent monomers requires simultaneous consideration of their electronic coupling, crystal lattice symmetry, and synthetic viability.[33] We addressed this through selection of an electron-rich pyrene building block and an electron-deficient thienoisoindigo linker with molecular orbital energy levels comparable to that of the semiconducting TMDCs.[22,33–35] We applied first-principles electronic structure calculations to several candidate structures (SI.I) and evaluated both the electronic structure and the synthetic viability to obtain a target 2DP (TIIP). TIIP is synthesized by condensing a tetrafunctionalized $D_{2h}$ symmetric pyrene (tetrakis(4-aminophenyl)pyrene, TAPPy) with a bifunctional thienoisoindigo (N,N′-dibutyl-6,6′-diformylthienoisoindigo) (Figure 1B and SI.V–VI), which forms a layered 2D crystal with lattice constant $a_1 = a_2 = 2.9$ nm. Our electronic structure calculations (Figure 1C and SI.II) predict that TIIP is a semiconductor in its bulk form with an indirect band gap of 1.38 eV. Calculations also predict that the charge density at the top of the TIIP valence band is delocalized across the unit cell (Figure 1D). Notably, the intralayer lattice constant of 2DPs (2.9 nm) will be nearly 10 times larger than the interlayer (π–π) spacing (3.5 Å), suggesting that the behavior of electrons in 2DP semiconductors could be dominated by interlayer coupling rather than intralayer coupling dynamics.

Although much of the interest in semiconducting 2DPs and vdW heterostructures is focused on the potential for device applications, the vast majority of semiconducting 2DPs are synthesized as microcrystalline powders and it remains a challenge to obtain homogeneous thin films with high materials quality.[36,37] To address this, we developed an optimized solvothermal synthesis that permits the direct growth of highly crystalline and oriented TIIP films directly on sapphire and monolayer TMDC substrates (Figure 1E and SI.XIV). To promote homogeneous and crystalline film growth, we selected conditions that minimized the homogeneous formation of powder precipitates while still allowing for heterogeneous nucleation at the desired interface and confirmed the resulting structures by Fourier-transform infrared spectroscopy (FTIR), nuclear magnetic resonance (NMR), and surface area analyses (SI.VI–VIII).[38] The optimized solvothermal synthesis was highly reproducible and amenable to a variety of substrates. Across substrates, this synthesis generated the highest quality TIIP films on monolayer TMDCs, where the film exhibits homogeneous preferential growth in both crystallinity

and thickness (SI.IX and SI.XIV). This observation is consistent with reports of preferential 2DP growth on graphene[39] and hexagonal boron nitride[40] and suggests that this synthesis provides a generalizable route to directly form strong interfaces between high- quality semiconducting 2DP films and monolayer TMDCs.

The resulting TIIP 2DP formed robust, homogeneous, and crystalline films, as observed through optical microscopy, transmission electron microscopy (TEM), X-ray scattering, and atomic force microscopy (AFM) (Figure 2). Optical micrographs show homogeneous large-area film growth on both sapphire ($Al_2O_3$) substrates and monolayer $MoS_2$ (Figure 1E). Grazing incidence wide-angle X-ray scattering (GIWAXS) exhibits sharp diffraction peaks at 0.21, 0.31, 0.43, and 1.76 $Å^{-1}$ corresponding to the 100, 110, 200, and 001 Bragg diffraction features

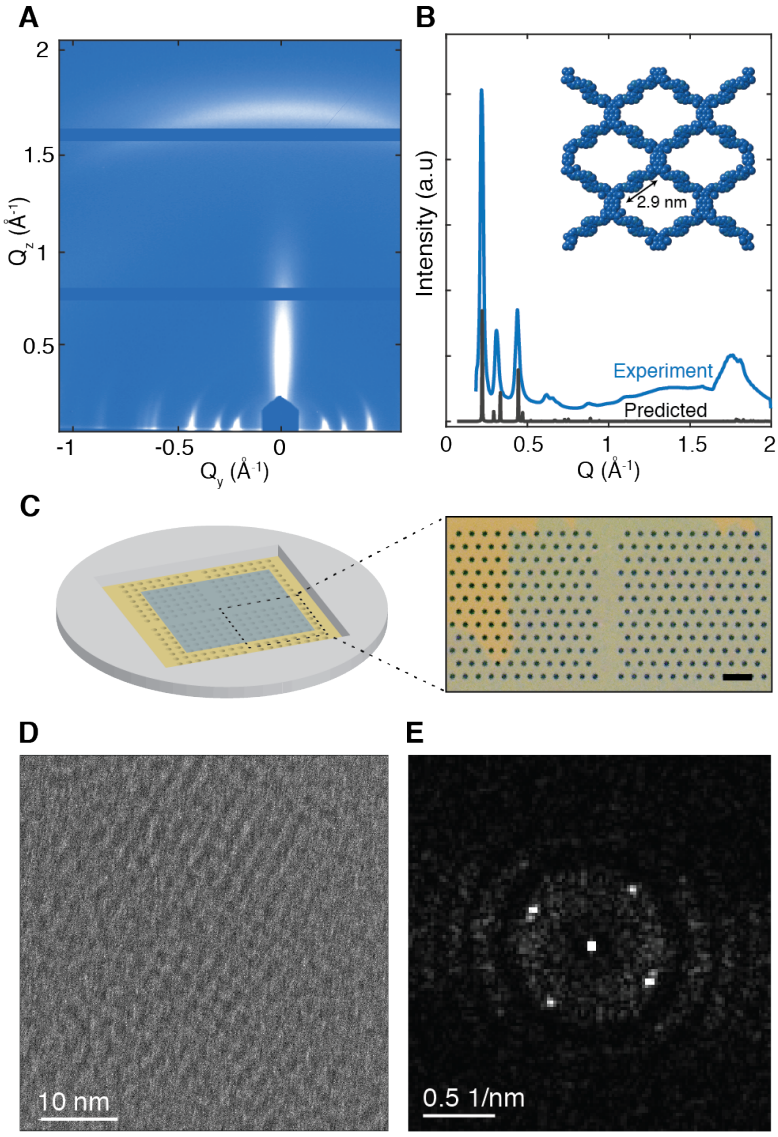


**Figure 2. Structural characterization of TIIP 2DP films. (A)** GIWAXS pattern from TIIP films confirm TIIP forms highly crystalline domains oriented parallel to the substrate. **(B)** Radial integration of the 2D GIWAXS (blue) and the simulated scattering pattern (black) indicate lattice constants a = 2.9 nm, c = 3.5 Å, consistent with theory. **(C)** Schematic of freestanding TIIP films (blue) transferred to a TEM grid. Right: optical micrograph of the TIIP film (blue) transferred to a TEM grid. Scale bar = 5$\mu$m. **(D)** HR-TEM image of the TIIP film resolves the orthorhombic lattice. **(E)** FFT of image in (D) resolves lattice symmetry.

(Figure 2A and 2B). These features correspond to lattice vectors of $a_1 = a_2 = 29.8$ Å and $c = 3.5$ Å and are in good agreement with a simulated orthorhombic 2DP structure (Figure 2B, black curve, and SI.VII) and the calculated TIIP structure (SI.II). Analysis of the angular dependence of the scattering intensity in the two-dimensional GIWAXS patterns shows that in-plane diffraction features are confined to the $Q_{xy}$ axis and out-of-plane diffraction features are tightly confined to the $Q_z$ axis. This strong radial anisotropy in the scattering intensity confirms that the TIIP 2DP crystal domains lie oriented parallel to the substrate. FTIR spectra of the TIIP films exhibit resonances consistent with a high degree of imine polymerization as well as a marked absence of resonances corresponding to oxidized species or unreacted constituent monomers (SI.VIII). Comparison of $^{13}C$ NMR of TIIP 2DP with its constituent starting materials and a model compound further indicates formation of the imine linkage (SI.VIII). Finally, TIIP 2DP was prepared as freestanding films on TEM grids using our all- dry film transfer method (SI.XI), which enabled direct imaging of the 2DP lattice at many film positions across the grid (Figure 2C−E and SI.XII). The Fourier-transform of the real space image confirms the orthorhombic symmetry of the TIIP 2D lattice and spacings consistent with the dimensions of the monomer subunits. Collectively, these results indicate that the TIIP 2DP achieves a prerequisite for electronically coupled 2DP/TMDC heterostructures: polymerization into large-area, homogeneous, highly crystalline, vdW-layered films that orient parallel to the substrate and form heterostructures of exceptionally high quality.

The synthesis of homogeneous crystalline vdW-layered films enabled us to probe the predicted low band gap and semiconducting electronic structure of the TIIP film. We characterized the electrical transport properties of the TIIP film using both prepatterned bottom contacts and large-area top contacts developed for transport on 2DP films (Figure 3A and SI.X). Across devices, we observe reproducible conductivities in the TIIP film of $\sigma = (3.5 \pm 0.7) \times 10{-}5$ S/m from the top contact geometry and $\sigma = (2.5 \pm 0.8) \times 10^{-5}$ S/ m from the bottom contact geometry, which is among the highest intrinsic electrical conductivity reported in 2D COFs (Figure 3B).[41−45] The optical band gap of the TIIP film can be determined through optical absorption measurements on sapphire substrates (Figure 3C), which shows an onset of optical absorption at 1.6 eV. The absorption onset energy of the 2DP film is red shifted by 300 meV from that of the thienoisoindigo monomer and by 100 meV from that of an imine-containing model compound (SI.V Figure S9). The decrease of the optical gaps in the extended TIIP structures reflect

the hybridization of the constituent monomers. In the TIIP/$MoS_2$ heterostructure, we observe additional absorption resonances corresponding to the $MoS_2$ A- and B-excitons (SI.XIII).[4] The low-energy optical gap of the TIIP film is indeed comparable to that of $MoS_2$, which would potentially enable charge and energy transfer processes in TIIP/$MoS_2$ heterostructures. Consistent with our theoretical results, these observations validate the theory-driven approach to designing semiconducting 2DPs.

Enabled by the synthesis of highly crystalline and oriented vdW films, we extended techniques from all-dry micro- mechanical manipulation of inorganic 2D materials to exfoliate the

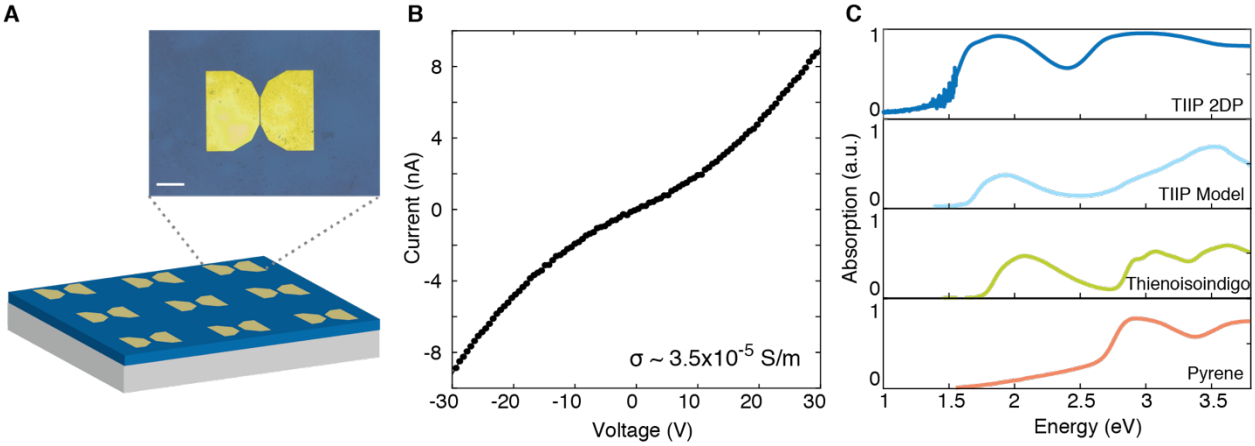


**Figure 3. Electrical and optical characterization of TIIP 2DP films. (A)** Schematic of a patterned TIIP device. Inset: optical micrograph of TIIP film (blue) with lithographically patterned Au top contacts (yellow). Scale bar = 50 $\mu$m. **(B)** Semiconducting electrical transport of TIIP films. I-V data of films exhibit an intrinsic conductivity of $\sigma \sim 3.5 \times 10^{-5}$ S/m. **(C)** Low-bandgap absorption of TIIP film, model compound, and monomers. The optical bandgap decreases in the extended TIIP film (dark blue) from that of the constituent monomers, reflecting the hybridization of electronic states in the extended lattice.

bulk TIIP films down to a few nanometers (Figure 4). Like semiconducting TMDCs, the 2DP layers are held in vertical alignment through relatively weak van der Waals forces. When the layered crystal is oriented parallel to the substrate, covalently bound sheets can, in principle, be separated by interrupting the interlayer van der Waals interactions. Conventionally, 2DPs are challenging to exfoliate or have been limited to liquid exfoliation due to their synthesis as polycrystalline powders, lack of a preferred orientation, or substantial intersheet cross-linking defects.[46–49] In contrast, the highly crystalline synthesis and oriented stacking in the TIIP 2DP films permits precise dry mechanical exfoliation of the 2DP TIIP film (Figure 4A). We exfoliated multiple TIIP layers from the bulk substrate-supported heterostructure (Figure 4B) using a polyethylene terephthalate (PET) stamp[50,51] controlled by a three-axis

micromanipulation translation stage (SI.XI). A single stamp exfoliation simultaneously removes layers from adjacent heterostructures leaving few-layered 2DP/TMDC heterostructures on the substrate (Figure 4C). AFM topography indicates that exfoliated heterostructures range from ∼2.5 to 10 nm and confirms that ultrathin TIIP films are continuous, uniform, and exhibit sub-nanometer surface roughness across the entire heterostructure area, which is free of bubbles or nanoscale impurities (SI.IX).

Exfoliation of TIIP 2DP sheets reveals a striking thickness dependence in the photoluminescence (PL) spectra (normalized by absorbed laser power, Figure 4D). The PL spectra (at 77 K, 2.33 eV excitation) exhibit a significant blue shift between the bulk and the ultrathin TIIP films: two weak and broad emission peaks centered at ∼1.4 and ∼1.6 eV are present in the bulk film, while a single resonance at 1.75 eV dominates the emission of the ultrathin film. In addition, the bulk TIIP film shows a very low PL quantum efficiency, consistent with our calculations that bulk TIIP has an indirect band gap. In contrast, the PL quantum efficiency increases by over 2 orders of magnitude in the few nanometer TIIP film.

The electronic structure of TIIP provides insight into the layer-dependent PL of the TIIP 2DP. In particular, the calculated valence band in TIIP 2DP has an in-plane bandwidth of 50 meV but an out-of-plane bandwidth of 400 meV along the stacking direction. This strong out-of-plane dispersion indicates that the electronic bands in TIIP can exhibit a strong thickness dependence, as observed in the enhancement of the PL. The strong enhancement in PL efficiency from ultrathin TIIP films is also reminiscent of the behavior in 2D semiconducting TMDCs, where the PL efficiency is greatly enhanced in monolayers due to an indirect-to-direct band gap transition.[3,4] However, the electronic structures of 2DPs exhibit unique properties relative to their inorganic counterparts, and the exact mechanism of layer-dependent PL emission in 2DPs requires further investigation. For example, in contrast to the TMDCs, the intralayer lattice constants of 2DPs, such as TIIP, are nearly an order of magnitude larger than the interlayer (π–π) spacing. The strong out-of-plane dispersion and relatively small in-plane bandwidth is one consequence of this feature and renders the electron interlayer coupling stronger than the electron intralayer coupling in such 2DPs.

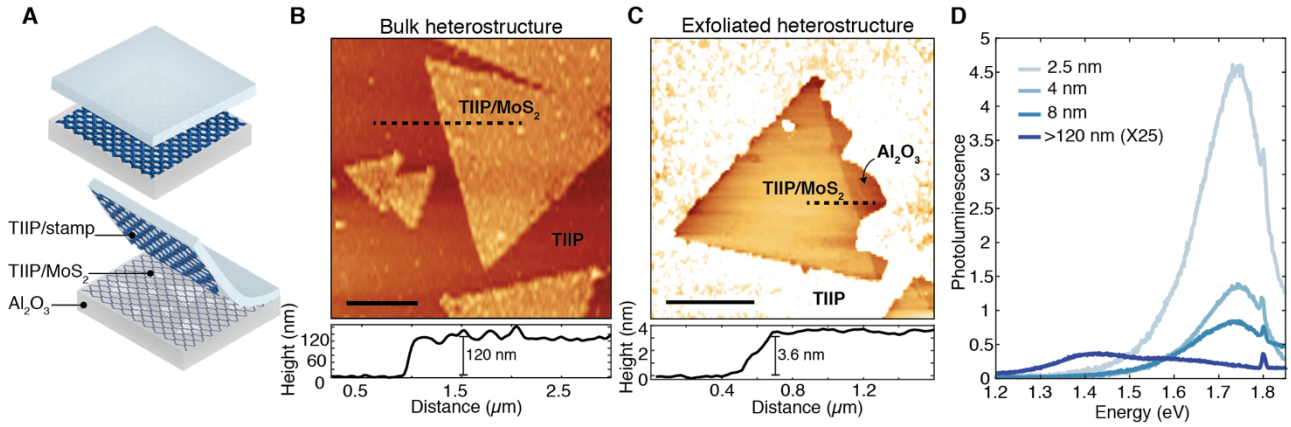


**Figure 4. Exfoliation of TIIP/$MoS_2$ heterostructures and thickness-dependent luminescence. (A)** Schematic of dry exfoliation of layered TIIP films. PET stamp is positioned above TIIP/$MoS_2$ heterostructure. Using micromechanical stamp exfoliation, the vdW layered TIIP films can be exfoliated down to few-nm sheets. **(B)** AFM topography of bulk layered TIIP/$MoS_2$ heterostructures. TIIP film covers both monolayer $MoS_2$ and the $Al_2O_3$ substrate but grows preferentially on the $MoS_2$. Below: AFM height profile of >120 nm bulk heterostructure. Scale bar = 2 $\mu$m. **(C)** AFM topography of exfoliated TIIP/$MoS_2$ heterostructures. Topographies trace the height from the exfoliated TIIP film to the bare sapphire substrate exposed in the exfoliation. Below: AFM height profile of heterostructure exfoliated to <4 nm. Scale bar = 2 $\mu$m. **(D)** PL spectra at 77 K for varying TIIP film thicknesses ranging from 2.5 nm to >120 nm. $\lambda_{exc}$ = 2.33 eV. Spectra are normalized by the absorbed laser power. Bulk (>120 nm, dark blue) TIIP is magnified by 25X for visual clarity.

The oriented synthesis and exfoliation of 2DP films in $MoS_2$ heterostructures offer a new degree-of-freedom to explore previously inaccessible interlayer coupling in semiconducting 2DPs. We use two independent methods to probe the ultrafast energy transfer dynamics between ultrathin TIIP and $MoS_2$ layers in the TIIP/$MoS_2$ heterostructure: photoluminescence excitation (PLE) spectroscopy and photo- luminescence (PL) quenching (Figure 5). In PLE, we monitor the emission from TIIP films as the excitation photon energy is swept across the energy range spanning the $MoS_2$ A- and B- exciton resonances. The resulting 2D PLE spectra of ultrathin TIIP/$MoS_2$ heterostructures expose two bright features where the emission of the TIIP has been enhanced at excitation energies of 1.9 and 2.1 eV (Figure 5A). While the TIIP absorption is relatively flat over this regime, these energies directly coincide with the well-known A- and B-exciton absorption of $MoS_2$ (SI.XIII). The enhancement of TIIP emission upon $MoS_2$ excitation provides direct evidence of an ultrafast energy transfer process from the $MoS_2$ layer to the TIIP layer through electronic coupling in the heterostructure.

The efficiency of this energy transfer can be quantitatively determined by comparing the PLE spectrum (Figure 5B, blue curve) to the absorption spectrum (Figure 5B, black curve). In the absorption spectrum, the A-exciton resonance of $MoS_2$ is much stronger than the broad TIIP absorption background with a resonance-to-background ratio of ~300%. In contrast, the $MoS_2$ A-exciton resonance shows only a ~60% enhancement over the background in the PLE spectrum, indicating that excitation of the $MoS_2$ A-exciton can contribute to the TIIP PL emission but does not contribute as efficiently as direct excitation of the TIIP layers. We can therefore estimate that the energy transfer efficiency the fraction of the optical absorption in $MoS_2$ that leads to TIIP excitation through energy transfer is limited to about 20%.

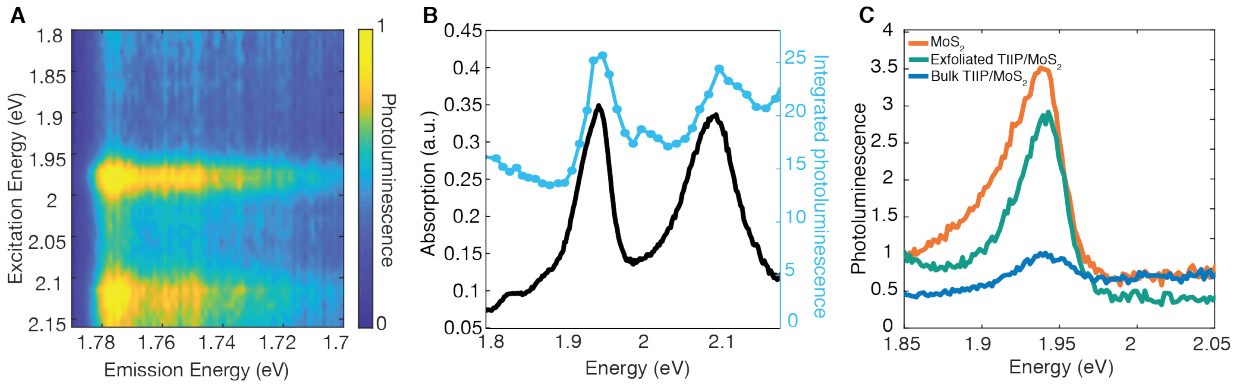


**Figure 5. Interlayer electronic coupling in 2DP TIIP/$MoS_2$ heterostructures. (A)** 2D PLE spectra of TIIP in ultrathin heterostructures at 77 K. The color scale represents the emission intensity. **(B)** Integrated PLE from TIIP (blue) and the heterostructure absorption (black). The enhancement of TIIP emission upon $MoS_2$ excitation reveals an ultrafast transfer process from $MoS_2$ to TIIP through interlayer electronic coupling in the heterostructure. **(C)** Quenching of $MoS_2$ PL in the TIIP/$MoS_2$ heterostructure can be tuned by TIIP thickness suggesting that interlayer dynamics can depend strongly on the thickness of the 2D TIIP layer.

A second and complementary estimation of the energy transfer efficiency can be obtained from the quenching of the $MoS_2$ emission due to the ultrafast energy transfer process. Figure 5C shows the PL emission from the $MoS_2$ A-exciton in bare $MoS_2$ (orange), the ultrathin TIIP/$MoS_2$ heterostructure (green), and the bulk TIIP/$MoS_2$ heterostructure (blue). In the ultrathin TIIP/$MoS_2$ heterostructure (green), emission from the monolayer $MoS_2$ A-exciton resonance (1.9 eV), prominent in isolation, is quenched by ~15% in the ultrathin heterostructure. This degree of quenching corresponds to an energy transfer efficiency of 15% and is comparable to the value estimated independently from PLE spectroscopy. In contrast, the A-exciton emission in the bulk

TIIP/$MoS_2$ heterostructure (blue) is strongly quenched and exhibits an energy transfer efficiency as high as 85%. Reproducible across numerous devices and in good agreement with the estimation from PLE spectroscopy, these results demonstrate that the excited state dynamics in TIIP/$MoS_2$ heterostructures can depend strongly on the thickness of the 2D TIIP layer.

The rate of energy transfer across the TIIP/$MoS_2$ heterostructure can be estimated from the respective energy transfer efficiencies. The energy transfer efficiency, $\eta$, is set by the competition between the exciton decay rate within $MoS_2$ ($\gamma_{MoS2}$) and the energy transfer rate to TIIP ($\gamma_{transfer}$) and is described by $\eta = \frac{\gamma_{transfer}}{\gamma_{MoS2}+\gamma_{transfer}}$. Studies of CVD-grown $MoS_2$ show that the $MoS_2$ total decay rate, $\gamma_{MoS2}$, is on the order of 1 $ps^{-1}$ [52], consistent with our time-resolved PL measurements of the exciton lifetime of the CVD-grown $MoS_2$, limited by the instrument response time of the streak camera (~2 ps). Thus, $\gamma_{MoS2}$ ~1 $ps^{-1}$ provides a useful bound for the $MoS_2$ total decay rate and the energy transfer rate can be estimated from the experimentally realized energy transfer efficiency for different 2DP thicknesses. Bulk TIIP/$MoS_2$ exhibits a high energy transfer efficiency of 85%, corresponding to an ultrafast energy transfer rate on the order of 6 $ps^{-1}$. In contrast, the transfer efficiency in ultrathin TIIP/$MoS_2$ at 15% is relatively low and corresponds to a dramatically reduced transfer rate of 0.2 $ps^{-1}$. Consequently, these results suggest that the process of energy transfer in the heterostructure slows by more than an order of magnitude with decreasing 2DP TIIP thickness. The strongly thickness-dependent energy transfer rates in TIIP/$MoS_2$ heterostructures is quite unexpected. These observations suggest that the excited state dynamics in the coupled 2DP/TMDC heterostructure may be linked to the intrinsic interlayer coupling of the 2DP, underscoring robust opportunities to design emergent phenomena in hybrid 2DP/TMDC heterostructures.

## Conclusion

In conclusion, we demonstrate that through high quality layered 2DP growth on monolayer TMDCs, it is possible to engineer electronically coupled hybrid vdW heterostructures that reveal unexpected ultrafast excited state dynamics. We deterministically design the electronic band structure of TIIP and demonstrate growth of oriented and crystalline semiconducting TIIP films and TIIP/$MoS_2$ heterostructures of extremely high quality. We confirm structural characterization

in both real and reciprocal space (GIWAXS, TEM, and AFM), and low band-gap electronic characterization through optical absorption and semiconducting electrical transport.

These advances enabled direct exfoliation of 2DP films and the first thickness-dependent study of hybrid 2DP/TMDC heterostructures, which offers a new degree-of-freedom to explore in low-dimensional 2DP physics. Thickness-dependent measurements reveal that 2DP PL efficiency can increase by over two orders of magnitude in few-nm TIIP films and suggest consequences of the lattice dimensions that may be broadly general to 2DPs. Surprisingly, the sub-picosecond energy transfer rate in the TIIP/$MoS_2$ heterostructure is also modulated by TIIP layer number, which indicates that the interlayer coupling of the 2DP is intrinsically linked to the excited state dynamics of the coupled heterostructure. This coordinated approach to band-design and the realization of electronically coupled semiconducting TIIP/$MoS_2$ heterostructures demonstrates that 2DPs represent a powerful route to engineering novel 2D heterostructures for optoelectronic applications. Finally, extending this work to 2DPs containing topologically nontrivial band structures could open rich opportunities for the design and control of strongly correlated electronic states[33,53] in hybrid vdW heterostructures.

**Associated Content**

**Supporting Information**

Electronic band structure of candidate structures, electronic band structure of TIIP 2DP, materials, instrumentation, experimental details, monomer and model compound synthesis, NMR spectra, mass spectroscopy, 2DP film synthesis and preparation, structural modeling of TIIP 2DP, 2DP film characterization: FT-IR, CP-MAS, 12C, solid state NMR spectra, N2 isotherm, BET plot, AFM surface analysis, transport measurements and fabrication, methods of exfoliation and transfer of layered 2DP films, additional TEM areas, absorption of $MoS_2$ and TIIP/ $MoS_2$ heterostructures, GIWAXS on additional TMDCs.

**Corresponding Author:** *Feng Wang – Department of Physics, University of California, Berkeley, CA 94720, USA; Email: fengwang76@berkeley.edu

**Author Information:**

† A.M.E., R.R.D., H.L., and R.L. contributed equally to this work.

**Acknowledgments:** We thank Yi Liu, Victoria Norman, Greg Stiehl, Shilong Zhao, Lindsey Young, and Sheng Wang. We thank Ming-Yang Li and Lain-Jong Li at King Abdullah University of Science and Technology (KAUST) for providing the transition metal dichalcogenide substrates.

**Competing interests**: The authors declare no competing interests.

**Data and materials availability:** All data is available in the main text or the supplementary materials.

**Funding sources:** This work was supported by the Army Research Office for a Multidisciplinary University Research Initiatives (MURI) award under grant W911NF-15-1-0447. A.M.E. and I.C. are supported by the Ryan Fellowship and the Northwestern University International Institute for Nanotechnology and by the NSF Graduate Research Fellowship [A.M.E. under grant DGE-1324585; I.C. under grant DGE-1842165]. J.L.B. and H.L. acknowledge support from the College of Science, University of Arizona. This research used resources of the Advanced Light Source, a DOE Office of Science User Facility under contract no. DE-AC02-05CH11231. Work at the Molecular Foundry was supported by the Office of Science, Office of Basic Energy Sciences, of the U.S. Department of Energy under Contract No. DE-AC02-05CH11231. This work made use of the IMSERC at Northwestern University, which has received support from the Soft and Hybrid Nanotechnology Experimental (SHyNE) Resource (NSF ECCS-2025633), the State of Illinois, and the International Institute for Nanotechnology (IIN), as well as the Keck-II, SPID, and EPIC facilities of Northwestern University's NUANCE Center, which has received support from the Soft and Hybrid Nanotechnology Experimental (SHyNE) Resource (NSF ECCS-2025633); the MRSEC program (NSF DMR-1720139) at the Materials Research Center; the International Institute for Nanotechnology (IIN); the Keck Foundation; and the State of Illinois, through the IIN. We acknowledge Gatan Inc., Pleasanton, CA, USA for the use of the K3-IS camera installed at the EPIC facility of Northwestern University's NUANCE Center. Research reported in this publication was supported in part by instrumentation provided by the Office of The Director, National Institutes of Health of the National Institutes of Health under Award Number S10OD026871. The content is solely the responsibility of the authors and does not necessarily represent the official views of the National Institutes of Health. This research used resources of the Advanced Photon Source (Sectors 5, 8, and 12), a U.S. Department of Energy (DOE) Office of Science User Facility operated for the DOE Office of Science by Argonne National Laboratory under Contract No. DE-AC02- 06CH11357. Portions of this work were performed at the DuPont-Northwestern-Dow Collaborative Access Team (DND-CAT) located at Sector 5 of the Advanced Photon Source (APS). DND-CAT is supported by Northwestern University, E.I. DuPont de Nemours & Co., and the Dow Chemical Company. Work at Cornell was performed in part at the Cornell NanoScale Facility, an NNCI member supported by the NSF (NNCI-1542081) and at the Cornell Center for Materials Research shared facilities, supported by the NSF MRSEC program (DMR-1719875).

## References

(1) Kim, J.; Jin, C.; Chen, B.; Cai, H.; Zhao, T.; Lee, P.; Kahn, S.; Watanabe, K.; Taniguchi, T.; Tongay, S.; Crommie, M. F.; Wang, F. Observation of Ultralong Valley Lifetime in WSe2/MoS2 Heterostructures. *Sci. Adv.* **2017**, *3* (7), 1–7. https://doi.org/10.1126/sciadv.1700518.

(2) Jin, C.; Ma, E. Y.; Karni, O.; Regan, E. C.; Wang, F.; Heinz, T. F. Ultrafast Dynamics in van Der Waals Heterostructures. *Nat. Nanotechnol.* **2018**, *13* (11), 994–1003. https://doi.org/10.1038/s41565-018-0298-5.

(3) Splendiani, A.; Sun, L.; Zhang, Y.; Li, T.; Kim, J.; Chim, C. Y.; Galli, G.; Wang, F. Emerging Photoluminescence in Monolayer MoS 2. *Nano Lett.* **2010**, *10* (4), 1271–1275.

https://doi.org/10.1021/nl903868w.
(4) Mak, K. F.; Lee, C.; Hone, J.; Shan, J.; Heinz, T. F. Atomically Thin MoS2: A New Direct-Gap Semiconductor. *Phys. Rev. Lett.* **2010**, *105* (13), 136805. https://doi.org/10.1103/PhysRevLett.105.136805.
(5) Hong, X.; Kim, J.; Shi, S. F.; Zhang, Y.; Jin, C.; Sun, Y.; Tongay, S.; Wu, J.; Zhang, Y.; Wang, F. Ultrafast Charge Transfer in Atomically Thin MoS2/WS2 Heterostructures. *Nat. Nanotechnol.* **2014**, *9* (9), 682–686. https://doi.org/10.1038/nnano.2014.167.
(6) Rivera, P.; Seyler, K. L.; Yu, H.; Schaibley, J. R.; Yan, J.; Mandrus, D. G.; Yao, W.; Xu, X. Valley-Polarized Exciton Dynamics in a 2D Semiconductor Heterostructure. *Science (80-. ).* **2016**, *351* (6274), 688–691. https://doi.org/10.1126/science.aac7820.
(7) Jin, C.; Regan, E. C.; Yan, A.; Iqbal Bakti Utama, M.; Wang, D.; Zhao, S.; Qin, Y.; Yang, S.; Zheng, Z.; Shi, S.; Watanabe, K.; Taniguchi, T.; Tongay, S.; Zettl, A.; Wang, F. Observation of Moiré Excitons in WSe2/WS2 Heterostructure Superlattices. *Nature* **2019**, *567* (7746), 76–80. https://doi.org/10.1038/s41586-019-0976-y.
(8) Tran, K.; Moody, G.; Wu, F.; Lu, X.; Choi, J.; Kim, K.; Rai, A.; Sanchez, D. A.; Quan, J.; Singh, A.; Embley, J.; Zepeda, A.; Campbell, M.; Autry, T.; Taniguchi, T.; Watanabe, K.; Lu, N.; Banerjee, S. K.; Silverman, K. L.; Kim, S.; Tutuc, E.; Yang, L.; MacDonald, A. H.; Li, X. Evidence for Moiré Excitons in van Der Waals Heterostructures. *Nature* **2019**, *567* (7746), 71–75. https://doi.org/10.1038/s41586-019-0975-z.
(9) Geng, K.; He, T.; Liu, R.; Dalapati, S.; Tan, K. T.; Li, Z.; Tao, S.; Gong, Y.; Jiang, Q.; Jiang, D. Covalent Organic Frameworks: Design, Synthesis, and Functions. *Chem. Rev.* **2020**, *120* (16), 8814–8933. https://doi.org/10.1021/acs.chemrev.9b00550.
(10) Lyle, S. J.; Waller, P. J.; Yaghi, O. M. Covalent Organic Frameworks: Organic Chemistry Extended into Two and Three Dimensions. *Trends Chem.* **2019**, *1* (2), 172–184. https://doi.org/10.1016/j.trechm.2019.03.001.
(11) Diercks, C. S.; Yaghi, O. M. The Atom, the Molecule, and the Covalent Organic Framework. *Science (80-. ).* **2017**, *355* (6328). https://doi.org/10.1126/science.aal1585.
(12) Bisbey, R. P.; Dichtel, W. R. Covalent Organic Frameworks as a Platform for Multidimensional Polymerization. *ACS Cent. Sci.* **2017**, *3* (6), 533–543. https://doi.org/10.1021/acscentsci.7b00127.
(13) Lohse, M. S.; Bein, T. Covalent Organic Frameworks: Structures, Synthesis, and Applications. *Adv. Funct. Mater.* **2018**, *28* (33).
(14) Colson, J. W.; Woll, A. R.; Mukherjee, A.; Levendorf, M. P.; Spitler, E. L.; Shields, V. B.; Spencer, M. G.; Park, J.; Dichtel, W. R. Oriented 2D Covalent Organic Framework Thin Films on Single-Layer Graphene. *Science (80-. ).* **2011**, *332* (6026), 228–231. https://doi.org/10.1126/science.1202747.
(15) Miner, E. M.; Fukushima, T.; Sheberla, D.; Sun, L.; Surendranath, Y.; Dincə, M. Electrochemical Oxygen Reduction Catalysed by Ni3 (Hexaiminotriphenylene)2. *Nat. Commun.* **2016**, *7*, 1–7. https://doi.org/10.1038/ncomms10942.
(16) Evans, A. M.; Parent, L. R.; Flanders, N. C.; Bisbey, R. P.; Vitaku, E.; Kirschner, M. S.; Schaller, R. D.; Chen, L. X.; Gianneschi, N. C.; Dichtel, W. R. Seeded Growth of Single-Crystal Two-Dimensional Covalent Organic Frameworks. *Science (80-. ).* **2018**, *361* (6397), 52–57. https://doi.org/10.1126/science.aar7883.
(17) Liu, K.; Qi, H.; Dong, R.; Shivhare, R.; Addicoat, M.; Zhang, T.; Sahabudeen, H.; Heine, T.; Mannsfeld, S.; Kaiser, U.; Zheng, Z.; Feng, X. On-Water Surface Synthesis of Crystalline, Few-Layer Two-Dimensional Polymers Assisted by Surfactant Monolayers.

*Nat. Chem.* **2019**, *11* (11), 994–1000. https://doi.org/10.1038/s41557-019-0327-5.
(18) Kory, M. J.; Wörle, M.; Weber, T.; Payamyar, P.; van de Poll, S. W.; Dshemuchadse, J.; Trapp, N.; Schlüter, A. D. Gram-Scale Synthesis of Two-Dimensional Polymer Crystals and Their Structure Analysis by X-Ray Diffraction. *Nat. Chem.* **2014**, *6* (9), 779–784. https://doi.org/10.1038/nchem.2007.
(19) Kissel, P.; Murray, D. J.; Wulftange, W. J.; Catalano, V. J.; King, B. T. A Nanoporous Two-Dimensional Polymer by Single-Crystal-to-Single-Crystal Photopolymerization. *Nat. Chem.* **2014**, *6* (9), 774–778. https://doi.org/10.1038/nchem.2008.
(20) Wan, S.; Gándara, F.; Asano, A.; Furukawa, H.; Saeki, A.; Dey, S. K.; Liao, L.; Ambrogio, M. W.; Botros, Y. Y.; Duan, X.; Seki, S.; Stoddart, J. F.; Yaghi, O. M. Covalent Organic Frameworks with High Charge Carrier Mobility. *Chem. Mater.* **2011**, *23*, 4094–4097. https://doi.org/10.1021/cm201140r.
(21) Jin, E.; Asada, M.; Xu, Q.; Dalapati, S.; Addicoat, M. A.; Brady, M. A.; Xu, H.; Nakamura, T.; Heine, T.; Chen, Q.; Jiang, D. Two-Dimensional Sp2 Carbon–Conjugated Covalent Organic Frameworks. *Science (80-. ).* **2017**, *357* (6352), 673–676. https://doi.org/10.1126/science.aan0202.
(22) Bessinger, D.; Ascherl, L.; Auras, F.; Bein, T. Spectrally Switchable Photodetection with Near-Infrared-Absorbing Covalent Organic Frameworks. *J. Am. Chem. Soc.* **2017**, *139* (34), 12035–12042. https://doi.org/10.1021/jacs.7b06599.
(23) Galeotti, G.; De Marchi, F.; Hamzehpoor, E.; MacLean, O.; Rajeswara Rao, M.; Chen, Y.; Besteiro, L. V.; Dettmann, D.; Ferrari, L.; Frezza, F.; Sheverdyaeva, P. M.; Liu, R.; Kundu, A. K.; Moras, P.; Ebrahimi, M.; Gallagher, M. C.; Rosei, F.; Perepichka, D. F.; Contini, G. Synthesis of Mesoscale Ordered Two-Dimensional π-Conjugated Polymers with Semiconducting Properties. *Nat. Mater.* **2020**, 1–7. https://doi.org/10.1038/s41563-020-0682-z.
(24) Zhong, Y.; Cheng, B.; Park, C.; Ray, A.; Brown, S.; Mujid, F.; Lee, J. U.; Zhou, H.; Suh, J.; Lee, K. H.; Mannix, A. J.; Kang, K.; Sibener, S. J.; Muller, D. A.; Park, J. Wafer-Scale Synthesis of Monolayer Two-Dimensional Porphyrin Polymers for Hybrid Superlattices. *Science (80-. ).* **2019**, *366* (6471), 1379–1384. https://doi.org/10.1126/science.aax9385.
(25) Müller, V.; Hinaut, A.; Moradi, M.; Baljozovic, M.; Jung, T. A.; Shahgaldian, P.; Möhwald, H.; Hofer, G.; Kröger, M.; King, B. T.; Meyer, E.; Glatzel, T.; Schlüter, A. D. A Two-Dimensional Polymer Synthesized at the Air/Water Interface. *Angew. Chemie Int. Ed.* **2018**, *57* (33), 10584–10588. https://doi.org/10.1002/anie.201804937.
(26) Eichhorn, J.; Strunskus, T.; Rastgoo-Lahrood, A.; Samanta, D.; Schmittel, M.; Lackinger, M. On-Surface Ullmann Polymerization via Intermediate Organometallic Networks on Ag(111). *Chem. Commun.* **2014**, *50* (57), 7680–7682. https://doi.org/10.1039/c4cc02757d.
(27) Dai, W.; Shao, F.; Szczerbiński, J.; McCaffrey, R.; Zenobi, R.; Jin, Y.; Schlüter, A. D.; Zhang, W. Synthesis of a Two-Dimensional Covalent Organic Monolayer through Dynamic Imine Chemistry at the Air/Water Interface. *Angew. Chemie Int. Ed.* **2016**, *55* (1), 213–217. https://doi.org/10.1002/anie.201508473.
(28) Zhou, D.; Tan, X.; Wu, H.; Tian, L.; Li, M. Synthesis of C−C Bonded Two-Dimensional Conjugated Covalent Organic Framework Films by Suzuki Polymerization on a Liquid–Liquid Interface. *Angew. Chemie - Int. Ed.* **2019**, *58* (5), 1376–1381. https://doi.org/10.1002/anie.201811399.
(29) Matsumoto, M.; Dasari, R. R.; Ji, W.; Feriante, C. H.; Parker, T. C.; Marder, S. R.; Dichtel, W. R. Rapid, Low Temperature Formation of Imine-Linked Covalent Organic Frameworks

Catalyzed by Metal Triflates. *J. Am. Chem. Soc.* **2017**, *139* (14), 4999–5002. https://doi.org/10.1021/jacs.7b01240.
(30) Matsumoto, M.; Valentino, L.; Stiehl, G. M.; Balch, H. B.; Corcos, A. R.; Wang, F.; Ralph, D. C.; Mariñas, B. J.; Dichtel, W. R. Lewis-Acid-Catalyzed Interfacial Polymerization of Covalent Organic Framework Films. *Chem* **2018**, *4* (2), 308–317. https://doi.org/10.1016/j.chempr.2017.12.011.
(31) Grill, L.; Hecht, S. Covalent On-Surface Polymerization. *Nature Chemistry*. Nature Research February 1, 2020, pp 115–130. https://doi.org/10.1038/s41557-019-0392-9.
(32) Cui, D.; Perepichka, D. F.; MacLeod, J. M.; Rosei, F. Surface-Confined Single-Layer Covalent Organic Frameworks: Design, Synthesis and Application. *Chem. Soc. Rev.* **2020**, *49* (7), 2020–2038. https://doi.org/10.1039/c9cs00456d.
(33) Thomas, S.; Li, H.; Zhong, C.; Matsumoto, M.; Dichtel, W. R.; Bredas, J. L. Electronic Structure of Two-Dimensional π-Conjugated Covalent Organic Frameworks. *Chem. Mater.* **2019**, *31* (9), 3051–3065. https://doi.org/10.1021/acs.chemmater.8b04986.
(34) Dou, L.; Liu, Y.; Hong, Z.; Li, G.; Yang, Y. Low-Bandgap Near-IR Conjugated Polymers/Molecules for Organic Electronics. *Chem. Rev.* **2015**, *115* (23), 12633–12665. https://doi.org/10.1021/acs.chemrev.5b00165.
(35) Wang, E.; Mammo, W.; Andersson, M. R. 25th Anniversary Article: Isoindigo-Based Polymers and Small Molecules for Bulk Heterojunction Solar Cells and Field Effect Transistors. *Adv. Mater.* **2014**, *26* (12), 1801–1826. https://doi.org/10.1002/adma.201304945.
(36) Wang, W.; Schlüter, A. D. Synthetic 2D Polymers: A Critical Perspective and a Look into the Future. *Macromol. Rapid Commun.* **2019**, *40* (1), 1800719. https://doi.org/10.1002/marc.201800719.
(37) Rodríguez-San-Miguel, D.; Montoro, C.; Zamora, F. Covalent Organic Framework Nanosheets: Preparation, Properties and Applications. *Chem. Soc. Rev.* **2020**, *49* (8), 2291–2302. https://doi.org/10.1039/c9cs00890j.
(38) Li, H.; Evans, A. M.; Castano, I.; Strauss, M. J.; Dichtel, W. R.; Bredas, J. L. Nucleation-Elongation Dynamics of Two-Dimensional Covalent Organic Frameworks. *J. Am. Chem. Soc.* **2020**, *142* (3), 1367–1374. https://doi.org/10.1021/jacs.9b10869.
(39) Colson, J. W.; Woll, A. R.; Mukherjee, A.; Levendorf, M. P.; Spitler, E. L.; Shields, V. B.; Spencer, M. G.; Park, J.; Dichtel, W. R. Oriented 2D Covalent Organic Framework Thin Films on Single-Layer Graphene. *Science (80-. ).* **2011**, *332* (6026), 228–231. https://doi.org/10.1126/science.1202747.
(40) Sun, B.; Li, J.; Dong, W.; Wu, M.; Wang, D. Selective Growth of Covalent Organic Framework Ultrathin Films on Hexagonal Boron Nitride. 1–12.
(41) Cai, S.; Zhang, Y.; Pun, A. B.; He, B.; Yang, J.; Toma, F. M.; Sharp, I. D.; Yaghi, O. M.; Fan, J.; Zheng, S.; Zhang, W.-G.; Liu, Y. Tunable Electrical Conductivity in Oriented Thin Films of Tetrathiafulvalene Based Covalent Organic Framework. *Chem. Sci.* **2014**, *5* (12), 4693–4700. https://doi.org/10.1039/C4SC02593H.
(42) Duhović, S.; Dincă, M. Synthesis and Electrical Properties of Covalent Organic Frameworks with Heavy Chalcogens. *Chem. Mater.* **2015**, *27* (16), 5487–5490. https://doi.org/10.1021/acs.chemmater.5b02358.
(43) Nath, B.; Li, W. H.; Huang, J. H.; Wang, G. E.; Fu, Z. H.; Yao, M. S.; Xu, G. A New Azodioxy-Linked Porphyrin-Based Semiconductive Covalent Organic Framework with I2 Doping-Enhanced Photoconductivity. *CrystEngComm* **2016**, *18* (23), 4259–4263.

https://doi.org/10.1039/c6ce00168h.
(44) Kim, S.; Choi, H. C. Light-Promoted Synthesis of Highly-Conjugated Crystalline Covalent Organic Framework. *Commun. Chem.* **2019**, *2* (1), 60. https://doi.org/10.1038/s42004-019-0162-z.
(45) Lakshmi, V.; Liu, C. H.; Rajeswara Rao, M.; Chen, Y.; Fang, Y.; Dadvand, A.; Hamzehpoor, E.; Sakai-Otsuka, Y.; Stein, R. S.; Perepichka, D. F. A Two-Dimensional Poly(Azatriangulene) Covalent Organic Framework with Semiconducting and Paramagnetic States. *J. Am. Chem. Soc.* **2020**, *142* (5), 2155–2160. https://doi.org/10.1021/jacs.9b11528.
(46) Uribe-Romo, F. J.; Dichtel, W. R. Polymers Stripped Down. *Nat. Chem.* **2012**, *4* (4), 244–245. https://doi.org/10.1038/nchem.1317.
(47) Bunck, D. N.; Dichtel, W. R. Bulk Synthesis of Exfoliated Two Dimensional Polymers Using Hydrazone Linked Covalent Organic Frameworks. *J. Am. Chem. Soc.* **2013**, *135* (40), 14952–14955. https://doi.org/10.1021/ja408243n.
(48) Wang, S.; Wang, Q.; Shao, P.; Han, Y.; Gao, X.; Ma, L.; Yuan, S.; Ma, X.; Zhou, J.; Feng, X.; Wang, B. Exfoliation of Covalent Organic Frameworks into Few-Layer Redox-Active Nanosheets as Cathode Materials for Lithium-Ion Batteries. *J. Am. Chem. Soc.* **2017**, *139* (12), 4258–4261. https://doi.org/10.1021/jacs.7b02648.
(49) Lange, R. Z.; Hofer, G.; Weber, T.; Dieter Schluter, A. A Two-Dimensional Polymer Synthesized through Topochemical [2 + 2]-Cycloaddition on the Multigram Scale. *J. Am. Chem. Soc.* **2017**, *139* (5), 2053–2059. https://doi.org/10.1021/jacs.6b11857.
(50) Wang, L.; Meric, I.; Huang, P. Y.; Gao, Q.; Gao, Y.; Tran, H.; Taniguchi, T.; Watanabe, K.; Campos, L. M.; Muller, D. A.; Guo, J.; Kim, P.; Hone, J.; Shepard, K. L.; Dean, C. R. One-Dimensional Electrical Contact to a Two-Dimensional Material. *Science (80-. ).* **2013**, *342* (6158), 614–617. https://doi.org/10.1126/science.1244358.
(51) Jin, C.; Kim, J.; Suh, J.; Shi, Z.; Chen, B.; Fan, X.; Kam, M.; Watanabe, K.; Taniguchi, T.; Tongay, S.; Zettl, A.; Wu, J.; Wang, F. Interlayer Electron-Phonon Coupling in WSe 2/HBN Heterostructures. *Nat. Phys.* **2017**, *13* (2), 127–131. https://doi.org/10.1038/nphys3928.
(52) Wang, H.; Zhang, C.; Rana, F. Ultrafast Dynamics of Defect-Assisted Electron-Hole Recombination in Monolayer MoS2. *Nano Lett.* **2015**, *15* (1), 339–345. https://doi.org/10.1021/nl503636c.
(53) Springer, M. A.; Liu, T. J.; Kuc, A.; Heine, T. Topological Two-Dimensional Polymers. *Chem. Soc. Rev.* **2020**, *49* (7), 2007–2019. https://doi.org/10.1039/c9cs00893d.

# Supplementary Information for

# Electronically Coupled 2D Polymer/$MoS_2$ Heterostructures

Halleh B. Balch, Austin M. Evans, Raghunath R. Dasari, Hong Li, Ruofan Li, Simil Thomas, Danqing Wang, Ryan P. Bisbey, Kaitlin Slicker, Ioannina Castano, Sangni Xun, Lili Jiang, Chenhui Zhu, Nathan Gianneschi, Daniel C. Ralph, Jean-Luc Brédas, Seth R. Marder, William R. Dichtel, Feng Wang*

Correspondence to: fengwang76@berkeley.edu

## Supplementary Table of Contents

# I. Electronic band structure of candidate structures

Two dimensional conjugated polymers are compelling candidates for rationally designed 2D material heterostructures because their properties can be tuned at the molecular level through choice of constituent molecules and linkage chemistries. To develop a systematic understanding of the role of the constituent molecules in the band structure design, we applied first-principles electronic structure calculations (at the density functional theory PBE0 level using the POB-TZVP basis set) to single 2D layers of candidate structures formed of the electron-rich pyrene and the low band gap acceptor, thienoisoindigo, which together form a donor-acceptor complex[1]. Thienoisoindigo has attracted considerable attention as an acceptor moiety in both linear and 2D systems. In addition, the energetically favorable attraction between the ketones and sulfur atoms in thienoisoindigo promotes a planar molecular backbone[2]. Pyrene has proven successful as a moderately electron-rich donor building block in other luminescent 2D polymer systems[3–5]. The three candidate structures differ by the inclusion of a pyrene and a thiophene moiety, respectively (Figure S1). While Candidate I was predicted to have the smallest electronic band gap, we determined that the compact chemical structure was likely to induce torsion along the molecular backbone and reduce the viability of highly crystalline growth of oriented planar sheets, critical to the generation of interlayer electronic coupling. In contrast, the lattice constant in Candidate II increases by nearly 30%, which substantially improves the synthetic viability of planar and oriented crystalline growth, as demonstrated in the main text. Candidate III is similar to that reported by Bessinger et al.[6]. The use of similar screening of candidate structures for electronic and synthetic insight will advance the development of rational, electronically addressable, 2D materials.

**Candidate I:**
DFT/PBE0 calculated band gap of 1.31 eV.
Lattice parameters: a1 = 20.7Å, a2 = 20.7 Å, α = 82°

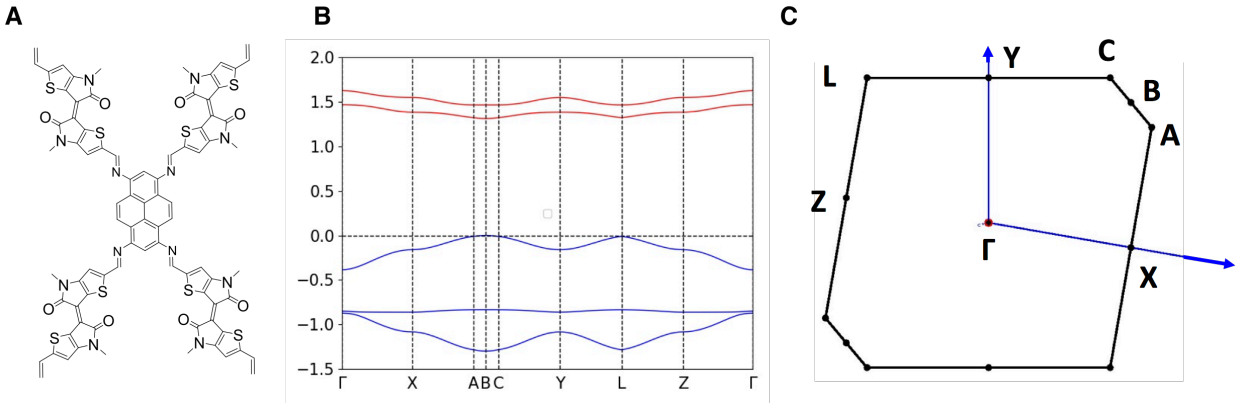


S 1. a) Candidate I chemical structure, b) Candidate I electronic band structure, c) Candidate I Brillouin zone.

**Candidate II:**
DFT/PBE0 calculated band gap: 1.88 eV
Lattice parameters: a1 = 29.2Å, a2 = 29.2 Å, α = 80°

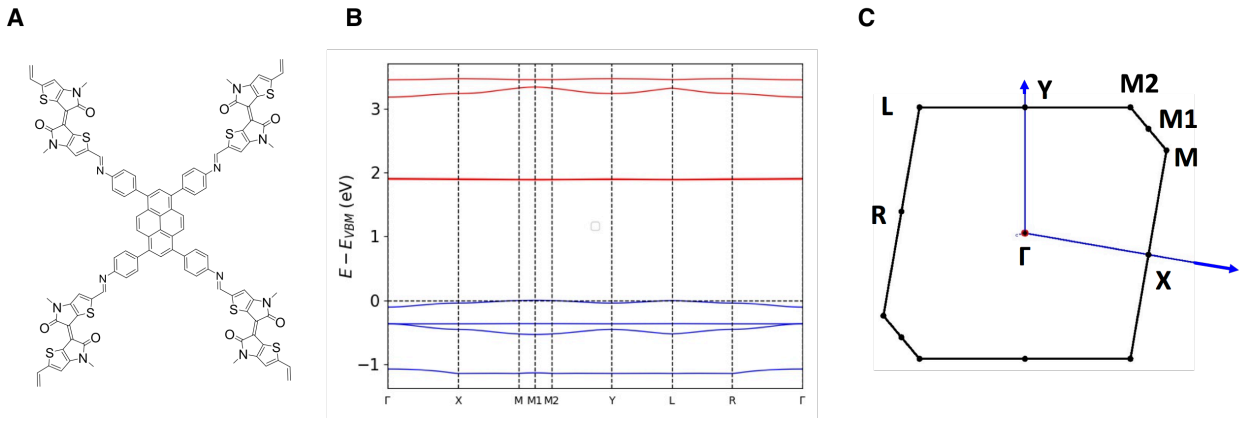


S 2. a) Candidate II chemical structure, b) Candidate II electronic band structure, c) Candidate II Brillouin zone.

**Candidate III:**

DFT/PBE0 calculated band gap: 1.94 eV

Lattice parameters: a1 = 38.17 Å, a2 = 38.17 Å, $\alpha = 100°$

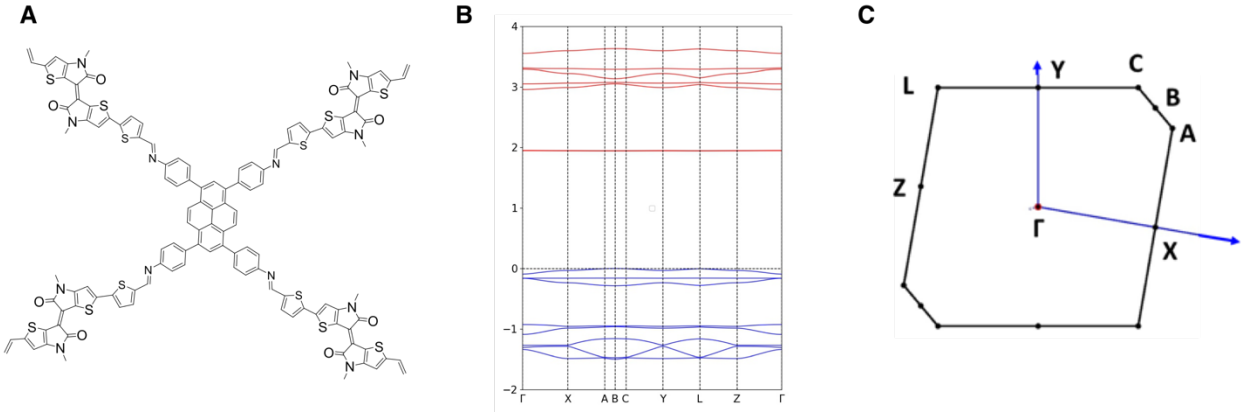


S 3. a) Candidate III chemical structure, b) Candidate III electronic band structure, c) Candidate III Brillouin zone.

# II. Electronic band structure of TIIP 2DP

The geometric and electronic properties of TIIP were calculated at the density functional theory PBE0 level with the CRYSTAL17 package. Our optimized bulk structure reveals a nearly eclipsed structure with an interlayer spacing of 3.2 Å and small in-plane displacements of 1.1 Å between neighboring layers along both *a1*- and *a2*-directions, with a1 = a2 = 29.2 Å.

**Multilayer TIIP 2DP**

Figure S4 shows the 3D Brillouin zone and associated electronic band structure of bulk TIIP 2DP. The valence band maximum occurs at the *M1* point and the conduction band minimum is along the out-of-plane *M1-H1* direction, which leads to the indirect nature of the 1.38 eV band gap. The hole effective mass in the bulk is calculated to be ~0.4$m_0$; the bandwidth around the valence band maximum in the out-of-plane direction (*M1-H1* direction) is ~400 meV. In contrast, the coupling in the in-plane *H1-Z* direction is about one order of magnitude weaker and results in a bandwidth of only ~50 meV. This value is about two times smaller than the bandwidth calculated for an isolated monolayer (Figure S5) –a consequence of electronic-polarization effects in the bulk. Thus, in contrast to TMDs, TIIP 2DP exhibits markedly stronger *inter*layer electronic coupling than *intra*layer coupling, which contributes to the observed layer dependent emission.

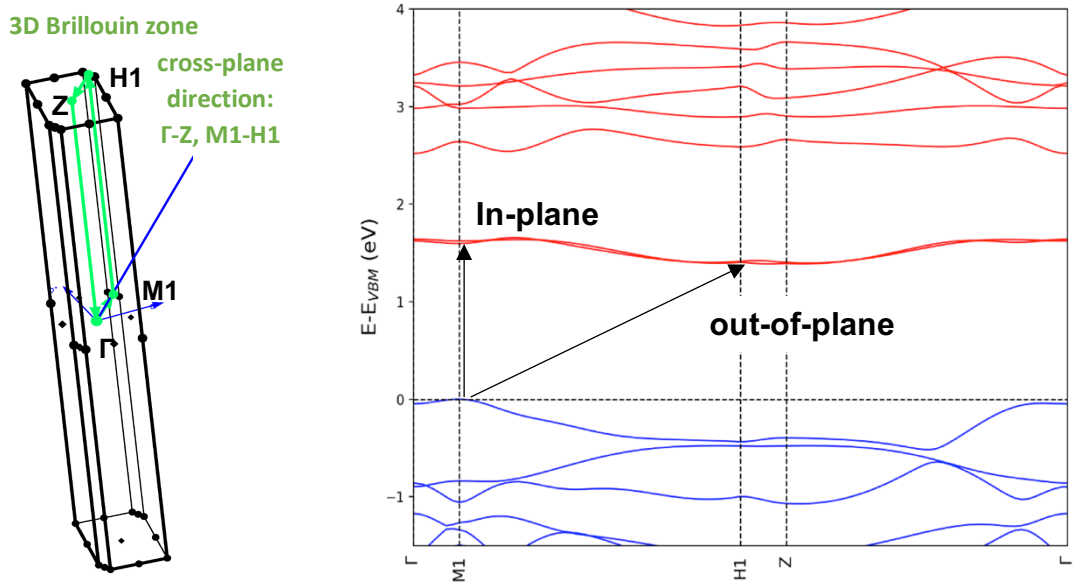


S 4. Electronic band structure of bulk TIIP (DFT/PBE0): (Left) the 3D Brillouin zone. (Right) the electronic band structure of bulk TIIP.

**Monolayer TIIP**

Electronic structure calculations of the monolayer 2D TIIP give a direct band gap of ~1.88 eV at the M1 point (Figure S5), with a valence bandwidth of ~110 meV.

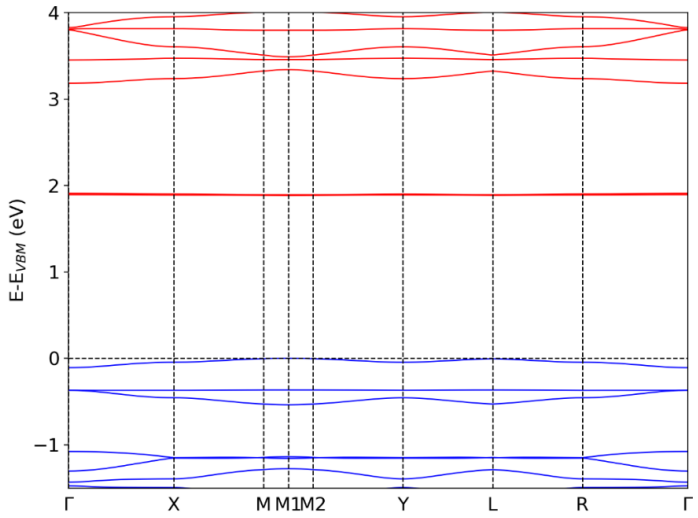


S 5. Electronic band structure of monolayer TIIP (DFT/PBE0).

**Heterostructure TIIP / $MoS_2$**

The TIIP/$MoS_2$ interface was modeled with a TIIP fragment adsorbed on monolayer $MoS_2$. Calculations at the DFT/PBE level indicate that the TIIP/$MoS_2$ interactions reduce the torsion angle between the pyrene and thienoisoindigo moieties by ~5˚. This coupling is observed via the sharp 110 peak in the GIWAXS data (Figure 2A-B) as well as in our DFT calculations.

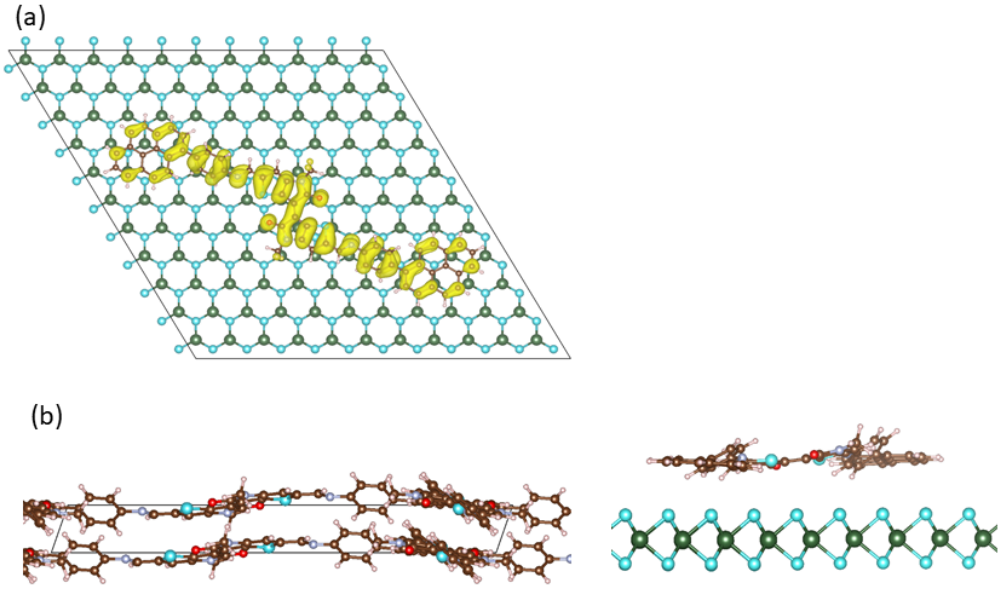


S 6. TIIP fragment on $MoS_2$: a) the charge density distribution at the valence band maximum (VBM). b) The interlayer coupling between the TIIP and $MoS_2$ reduces torsion in the coupled system.

# III. Materials

All reagents and solvents were purchased from commercial sources and used without further purification. 1-Bromopyrene was purchased from Fischer Scientific and used without additional purification. 4-Aminophenylboronic acid pinacol ester was purchased from Matrix Scientific. Scandium(III)triflate was purchased from Sigma-Aldrich. Dichlorobenzene, n-butanol, mesitylene and glacial acetic acid used in TIIP 2DP syntheses were all purchased from Fisher-Scientific and used without further purification. Deionized water was used to prepare 9 M acetic acid.

# IV. Instrumentation

**Nuclear Magnetic Resonance Spectroscopy.** $^{1}H$ and $^{13}C$ NMR spectra were acquired on Varian Mercury 300 MHz and Bruker AvanceIII 500 MHz equipped with a DHC CryoProbe and recorded at 25 °C. The spectra were calibrated using residual solvent as internal reference ($CDCl_3$: 7.26 ppm for $^{1}H$ NMR, 77.00 for $^{13}C$ NMR).

**Solid-state Nuclear Magnetic Resonance Spectroscopy.** Solid state $^{13}C$ CP/MAS NMR spectra of TIIP 2DP were recorded on a Varian 400 MHz at a spin rate of 10,000 Hz and calibrated using adamantane as an external standard.

**High Resolution Mass Spectrometry.** High-resolution mass spectra were acquired on an Applied Biosystems 4700 Proteomics Analyzer using MALDI or a Micromass AutoSpec M using electron impact (EI) mode. The mass spectra of a few samples were also acquired on Agilent 6210A LC-TOF Mass Spectrometer, with Atmospheric Pressure Photoionization (APPI) as an ionization source. The instrument is equipped with an Agilent Series 1200 HPLC binary pump, and Autosampler, using Mass Hunter software. The samples were run using direct injection.

**Elemental Analysis.** Elemental analyses were performed by Robertson Microlit Laboratories and by Atlantic Microlabs using a LECO 932 CHNS elemental analyzer.

**Infrared Spectroscopy of TIIP 2DP.** Infrared spectra were recorded on (1) a Nicolet iS10 FT- IR spectrometer equipped with a ZnSe ATR attachment and are uncorrected and (2) using Shimadzu IRPrestige-21 Fourier Transform Infrared Spectrophotometer or a Thermo Nicolet Avatar 360 FT-IR instrument in ATR mode using a Ge window (SpectraTech).

**Gas Sorption Isotherms.** Nitrogen sorption isotherms were conducted on a Micromeritics ASAP 2420 Accelerated Surface Area and Porosity Analyzer. Typically, 20-50 mg of powder TIIP 2DP were transferred to dried and tared analysis tubes equipped with filler rods and capped with a Transeal. The samples were heated to 40 °C at a rate of 1 °C $min^{-1}$ and evacuated at 40 °C for 20 min, then heated to 100 °C at a rate of 1 °C $min^{-1}$ heat, and evacuated at 100 °C until the outgas rate was ≤0.3 μmHg/min (holding the samples at 100 °C for 5 h was sufficient), at which point the tube was weighed again to determine the mass of the activated sample. The tube was then transferred to the analysis port of the instrument. UHP-grade (99.999% purity) $N_2$ was used for all adsorption measurements. $N_2$ isotherms were generated by incremental exposure to nitrogen up to 760 mmHg (1 atm) in a liquid nitrogen (77 K) bath. Oil-free vacuum pumps and oil-free pressure regulators were used for all measurements. Brunauer-Emmett-Teller (BET) surface areas were calculated from the linear region of the $N_2$ isotherm at 77 K within the pressure range $P/P_0$ of 0.05 – 0.10.

**Critical Point Dryer.** The supercritical drying procedure was performed in Tousimis Samdri795 critical point dryer. To keep the samples hydrated, samples were placed in a porous filter paper envelope (e.g. a tea bag) and soaked in IPA (typically 5-15 min). The drying chamber was first cooled (‘cool’ valve meter set to 0.40), and the envelopes containing the samples were placed inside, after which the chamber is filled with HPLC-grade IPA (>99.9%) and then sealed. The chamber was then filled with liquid $CO_2$ (‘fill’ valve meter set to 0.40), and after 2 min, the

chamber and samples were purged for 30 min ('purge-vent' valve meter set to 0.15, and 'purge timer' valve meter set to 6). The temperature was then raised to 40 °C resulting in a chamber pressure of approximately 1300 psi, which is above the critical point of $CO_2$. The chamber was held above the critical point for 30 min, after which the $CO_2$ source was turned off, and the pressure was released over a period of 30 min ('bleed' valve meter set at 0.07).

**Sonication.** Sonication was performed with a Branson 3510 ultrasonic cleaner with a power output of 100W and a frequency of 42 kHz.

**Transmission Electron Microscopy.** TEM was performed using a JEOL (JEOL USA, Inc., Peabody, MA) ARM300F GrandARM TEM operating at 300 keV equipped with a Gatan (Gatan, Inc., Pleasanton, CA) K3-IS "direct electron" detector.

**Grazing Incidence Wide-Angle X-ray Scattering.** Grazing-incidence X-ray wide-angle scattering (GI-WAXS) data was collected at the Advanced Light Source Lawrence Berkeley National Lab (ALS-LBNL) and at the Advanced Photon Source Argonne National Lab (APS-ANL).

ALS-LBNL: Beamline 7.3.3 with a photon energy of 10 keV ($\lambda$ = 1.24 Å). All measurements took place under a He atmosphere at ambient temperatures to minimize atmospheric scattering. Data was collected by a Dectris Pilatus 2M detector with a pixel size of 0.172 × 0.172 mm and 1475 × 1679 pixels was used to capture the 2D scattering patterns at a distance of 300mm from the sample. A silver behenate standard was used as a calibrant. The grazing angle, $\alpha$, was varied from 0.08° to 0.25°. Data was analyzed using the Nika macro for Igor Pro[8].

APS-ANL: Sector 8 of the Advanced Photon Source Argonne National Lab with a photon energy of 10.92 keV ($\lambda$ = 1.127 Å). Prior to measurement, all samples were placed under vacuum to remove atmospheric scatter. All patterns were collected with an incident angle of $\alpha$ = 0.14°. Frames were taken on a Pilatus 1M camera. The exposure time and amount of attenuation was tuned to provide 80% max saturation of any pixel on the Pilatus detector. Radial linecuts of the data were collected by radially integrating along the q axis using GIXSGUI[7].

**Atomic Force Microscopy.** Atomic force microscopy (AFM) scans were obtained on a Bruker Innova AFM in tapping mode.

**Linear Absorption Spectra.** Reflection contrast measurements of the TIIP/$MoS_2$ heterostructure were obtained under vacuum at 77K on a home-built reflection microscopy setup using a pulsed supercontinuum laser source (SC-PRO, YSL Photonics) using a 4 MHz repetition rate and a 50X objective. The incident light was focused on individual heterostructure flakes and focused to a diffraction-limited spot size of ~2 μm enabling addressing of individual heterostructures. The reflected light, R, was collected by the same objective and deflected by a beam splitter to a monochromator (Acton SP-2300i, Princeton Instruments) using a 150 g $mm^{-1}$ grating and equipped with a TE-cooled silicon CCD camera (iDus 420 Series, Andor). A reference spectrum, $R_0$, was taken on the sapphire substrate next to the sample. The normalized reflection contrast signal, ($R-R_0/R_0$), is directly proportional to the linear absorption from thin layers on sapphire [9]. Transmission contrast measurements ($T- T_0/ T_0$) of monomer, model, and bulk TIIP films (Figure 3C) were

obtained at room temperature by a Varian 5000 UV-Vis-NIR spectrometer. The reference spectrum, $T_0$, was obtained on a blank $Al_2O_3$ substrate. Spectra are plotted as $1-(T- T_0/ T_0)/100$, where $(T- T_0/ T_0)$ is proportional to the linear absorption from thin layers. Absorption maxima were determined from fits of the linear absorption spectra. The onset of absorption is taken conservatively to be the FWHM at the low-energy edge.

**Photoluminescence.** Photoluminescence measurements were obtained at 77K under constant absorbed light intensity using the reflection geometry in the confocal microscopy setup described above. 2.33 eV (532 nm) laser light (Diode-pumped solid state, Laserglow) was focused on the individual heterostructures with a diffraction-limited ~2 μm beam spot and power limited to <22 μW, significantly below the threshold for sample damage. Photoluminescence spectra were collected and analyzed with a monochromator (Acton SP-2300i, Princeton Instruments) and a TE-cooled CCD camera (iDus 420 Series, Andor). Measurements repeated across heterostructures confirmed reproducibility. TIIP photoluminescence spectra were normalized to excitation power, integration time, and sample thickness.

**Photoluminescence Excitation (PLE).** PLE measurements were performed at 77 K using a pulsed supercontinuum laser source (SC-PRO, YSL Photonics), which was spectrally filtered by a grating and appropriate filters to provide a tunable excitation energy. Measurements were taken under the same reflection geometry as described above. The excitation light was focused at the sample with a diffraction-limited ~2 μm beam spot. Photoluminescence was collected at each excitation energy and analyzed with a monochromator (Acton SP-2300i, Princeton Instruments) and a TE-cooled CCD camera (iDus 420 Series, Andor). Each PL spectrum was normalized to the excitation power (<22 μW) and integration time. The photoluminescence intensity scaled linearly with excitation power for all energies studied. The integrated photoluminescence excitation intensity was integrated over a well-separated narrow band and plotted as a function of excitation energy.

# V. Monomer and model compound synthesis, NMR, Mass Spectrometry

In the TIIP 2DP described in the main text, we employ 1,3,6,8-tetrakis(4-aminophenyl)pyrene and *N*, *N*′-dibutyl-6,6'-diformylthienoisoindigo as donor and acceptor building blocks, respectively, to synthesize the imine-linked, semiconducting, low band gap 2D TIIP. We incorporate formyl end groups on the thienoisoindigo unit for imine functionalization and butyl groups to aid solubility during 2DP film formation. *N*,*N*′-Dibutyl-6,6'-diformylthienoisoindigo was synthesized as reported in our recent work[10] and purified extensively via column chromatography and recrystallization (Figure S7). We synthesized 1,3,6,8-tetrakis(4-aminophenyl)pyrene according to the procedures reported in supplementary ref.11 (Figure S8). TIIP model compound, bis(pyrenyl)thienoisoindigo, **2**, was synthesized as illustrated in Figure S9.

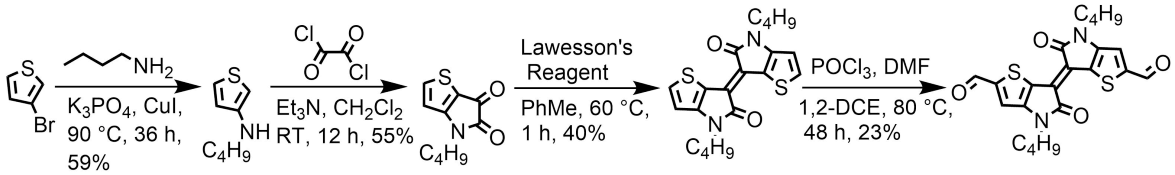


S 7. Synthesis of thienoisoindigo: thienoisoindigo dialdehyde linker.

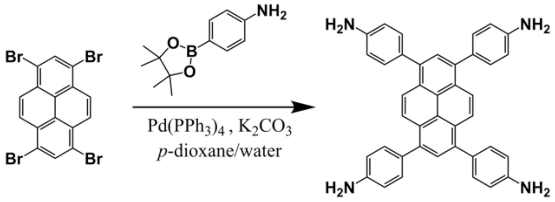


S 8. Synthesis of pyrene: tetraphenylpyrene amine node.

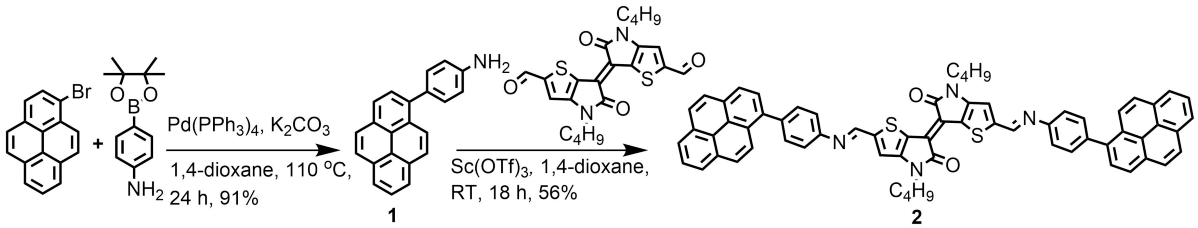


S 9. Synthesis of model: bis(pyrenyl)thienoisoindigo model compound.

**Synthesis of Pyrene: 1-(*p*-Aminophenyl)pyrene, 1**: A mixture of 1-bromopyrene (2.00 g, 7.11 mmol), 4-aminophenylboronic acid pinacol ester (2.40 g, 10.67 mmol), $K_2CO_3$ (1.93 g, 14.22 mmol), $Pd(PPh_3)_4$ (0.82 g, 0.71 mmol), 1,4-dioxane (30 mL) and de-gassed $H_2O$ (8 mL) was heated at 110 °C for 28 h. Upon completion, $H_2O$ (100 mL) was added into the reaction mixture and the crude product was extracted into $CH_2Cl_2$ (2 × 100 mL). The organic phase was washed with brine (150 mL), dried over anhydrous $Na_2SO_4$, and concentrated under reduced pressure. The crude product was purified by column chromatography (silica gel, 80:20, v/v, dichloromethane/hexanes) to afford product as a yellow solid. Yield: 1.9 g (91%). $^1$H NMR ($CDCl_3$, 300 MHz) δ 8.30-8.13 (m, 4H), 8.083 (d, $J$ = 0.9 Hz, 2H), 8.06-7.95 (m, 3H), 7.46 (dd, $J$ = 8.4, 1.8 Hz, 2H), 6.88 (dd, $J$ = 8.4, 1.8 Hz), 3.81 (s, br, 2H). $^{13}$C{$^1$H} NMR (75 MHz, $CDCl_3$) δ 145.6, 137.9, 131.5, 131.4, 131.3, 131.0, 130.1, 128.5, 127.6, 127.4, 127.1, 127.0, 125.8, 125.5,

125.0, 124.9, 124.8, 124.6, 124.5, 114.9. HRMS (EI) m/z calcd for $C_{22}H_{15}N$ (M+), 293.1204; found, 293.1206. Anal. Calcd for $C_{22}H_{15}N+_{1/8}H_2O$: C, 89.39; H, 5.20; N, 4.74. Found: C, 89.59; H, 5.52; N, 4.75.

**Synthesis of Thienoisoindigo Model Compound: bis(pyrenyl)thienoisoindigo, 2**. A 50 mL 2-neck flask was charged with *N*,*N*′-dibutyl-6,6'-diformylthienoisoindigo (0.04 g, 0.09 mmol), 1-(*p*-Aminophenyl)pyrene (**1**) (0.10 g, 0.27 mmol), and scandium(III) trifluoromethanesulfonate (0.005 g, 0.009 mmol). Under $N_2$, dioxane (5.0 mL) was added, and the resulting mixture was stirred at RT for 18 h. Upon completion, volatile solvents were removed under reduced pressure, methanol (30 mL) was added into the reaction mixture, and the resulting precipitate was collected *via* filtration. The precipitate was dissolved in hot toluene, filtered to remove any undissolved solids, and the filtrate was concentrated. The crude product was purified *via* multiple recrystallizations from toluene to afford the desired product. Yield: 0.05 g (56%). $^1$H NMR (1,1,2,2-tetrachloroethane-$d_2$, 300 MHz, 100 ºC) δ 8.81 (s, 2H), 8.31-8.8.20 (m, 8H), 8.18-8.04 (m, 10H), 7.76 (dd, *J* = 9.6, 1.8 Hz, 4H), 7.57 (dd, *J* = 8.4, 2.1 Hz, 4H), 7.34 (s, 2H), 3.96 (t, *J* = 6.0 Hz, 4H), 1.89 (pent, *J* = 6.9 Hz, 4H), 1.60-1.51 (m, 4H), 1.10 (t, *J* = 9.0 Hz, 6H). HRMS (MALDI) m/z calcd for $C_{66}H_{48}N_4O_2S_2$ (M+), 992.3219; found, 992.3230. Anal. Calcd for $C_{66}H_{48}N_4O_2S_2$+2$H_2O$: C, 77.02; H, 5.09; N, 5.55. Found: C, 77.34; H, 4.94; N, 5.49.

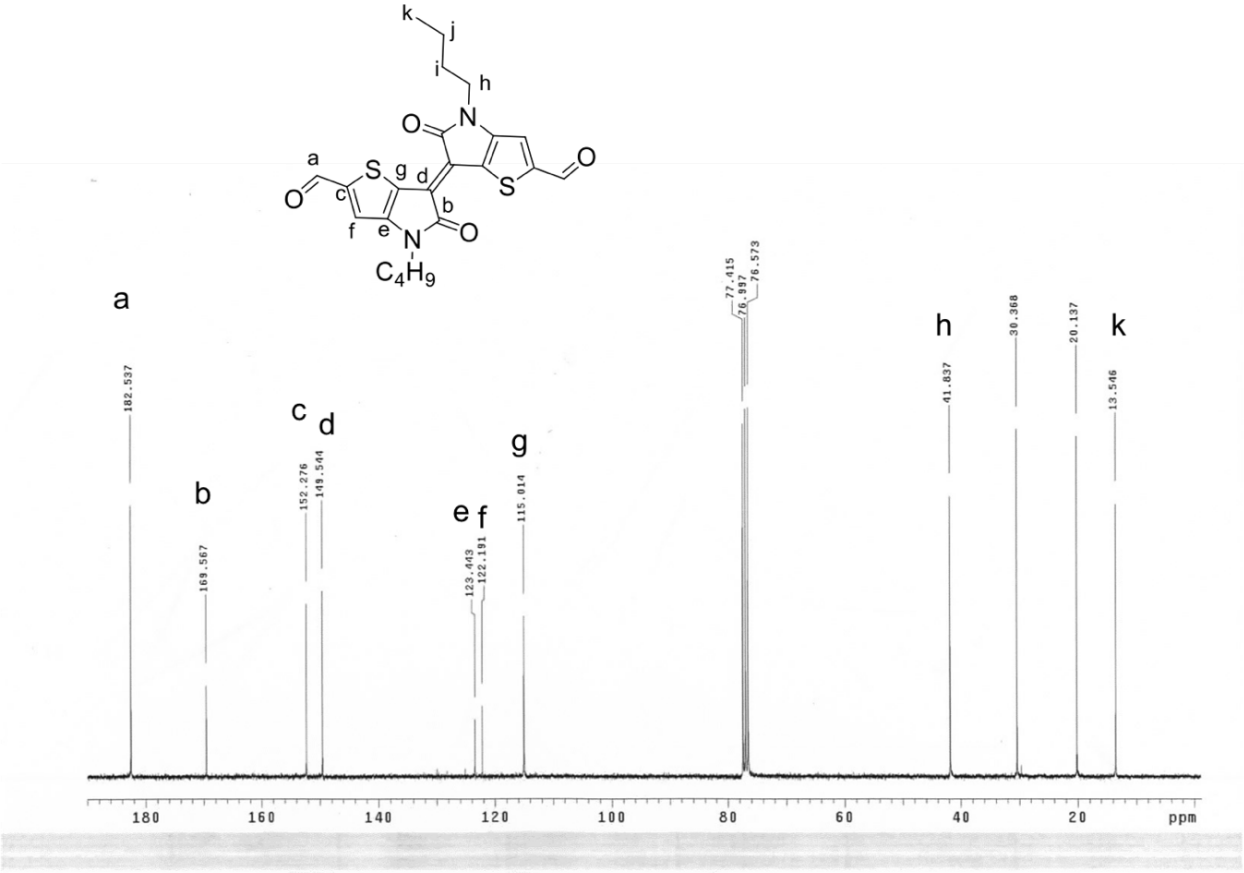


S 10. $^{13}$C NMR spectrum of thienoisoindigo with respective assignments (resonances around 77 ppm are due to residual solvent, $CHCl_3$).

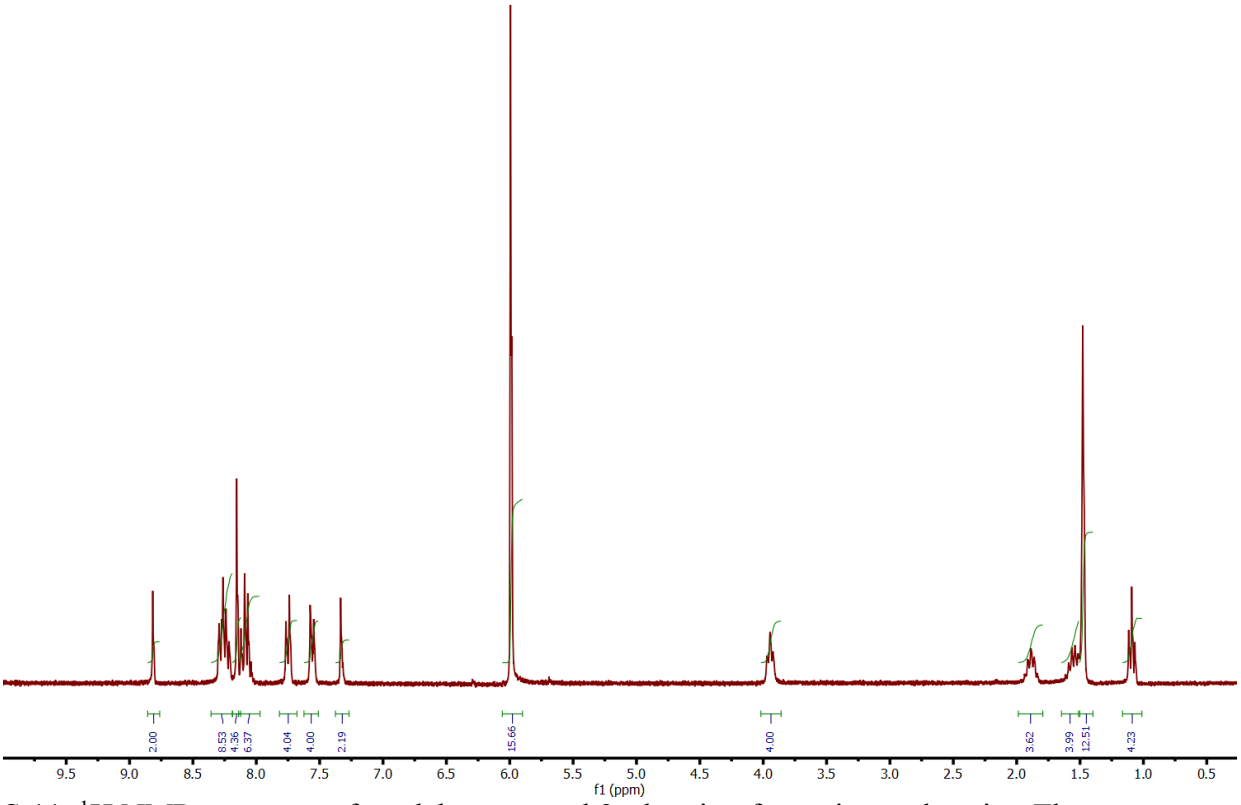


S 11. $^{1}$H NMR spectrum of model compound **2**, showing formation and purity. The resonance at 6 ppm is due to residual solvent, 1,1,2,2-tetrachloroethane.

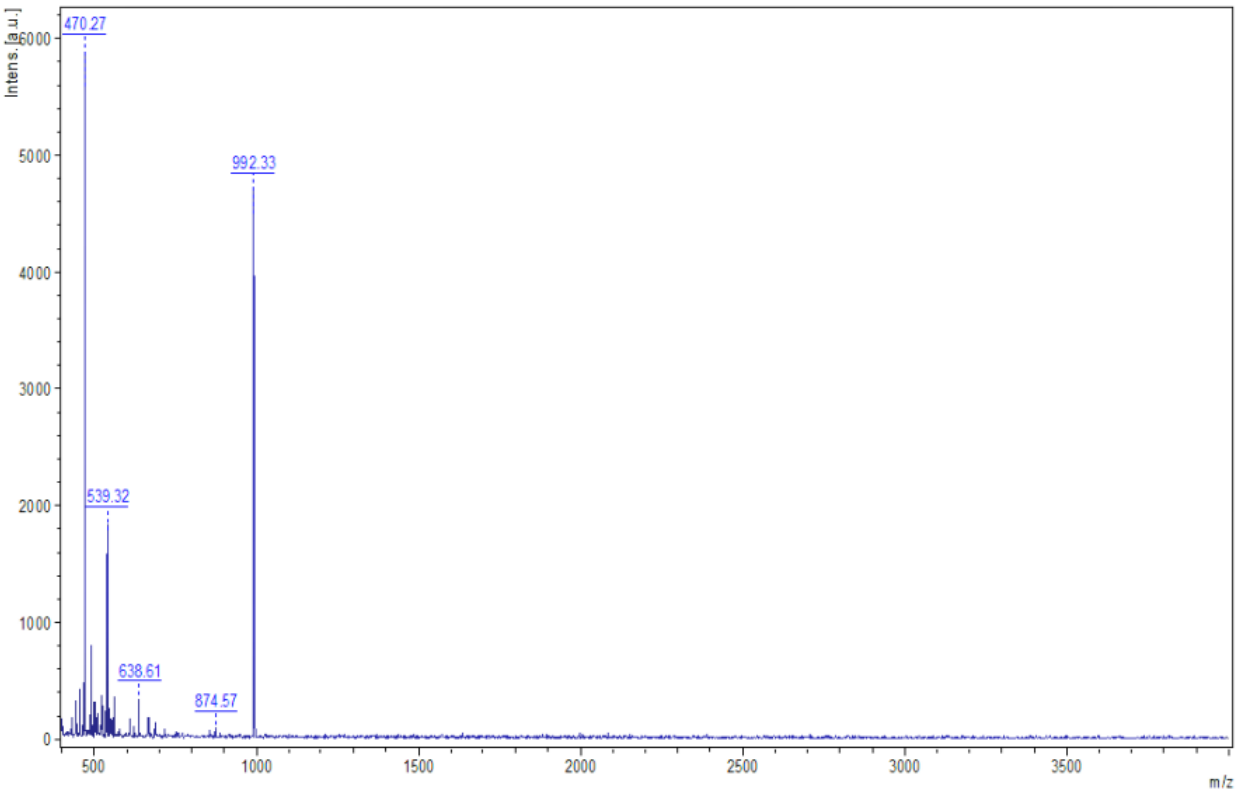


S 12. Mass spectrum of model compound **2**, showing molecular ion (m/z 992).

# VI. 2DP Film synthesis and workup

**Film Synthesis**

Direct polymerization of the monomer precursors on substrates in a solvothermal reaction chamber yielded highly crystalline and oriented films. Notably, in contrast to linear condensation polymerizations, 2DP polymerizations can achieve near-complete conversion and form high-quality 2DP by dynamic condensation chemistries, even in the presence of an excess of monofunctional monomers[12,13]. Mechanistic studies of 2DP polymerization[14–17] suggest that this advantage of 2DP polymerization is grounded in the reversibility of dynamic condensation chemistries which permits the iterative removal of defects from the global structure and thereby obtains a highly crystalline structure under optimized reaction conditions.

Through a screen of solvents, we found that a ternary solvent blend of 5:5:2 volume o-dichlorobenzene:n-butanol:mesitylene (20 mL total volume) well-solubilized the monomeric species. We further find that by optimizing catalyst loading, temperature, monomer concentration, we were able to preferentially form oriented 2DP film on the substrate and minimize the formation of powder precipitates during film growth, which can form inclusion defects. Stoichiometrically, tetra(4-aminophenyl)pyrene (TAPPy) co-crystallizes with p-dioxane during recrystallization[11] and we included this additional mass in our stoichiometric calculations.

We found the optimal reaction mixture to be TAPPy (2 mM, 1 equiv., 28 mg) and thienoisoindigo dialdehyde (TII-DA, 4 mM, 2 equiv., 35 mg) with 5 vol% (500 microliters) 9M acetic acid which we dissolved in 5:5:2 volume o-dichlorobenzene:n-butanol:mesitylene (20 mL total volume). These reactants were then sealed in the presence of a substrate (e.g. $Al_2O_3$, CVD-$MoS_2/Al_2O_3$, CVD-$WSe_2/Al_2O_3$, substrate size: ~1 mm X 3 mm X 0.5 mm) placed face-up in the reaction vessel, heated to 100 °C for 72 hours. During this time, a green film was found to conformally coat the inside of the reaction vessel and the immersed substrate.

**Film Workup**

Post-synthesis, we remove unreacted starting materials, residual catalyst, and TIIP powder precipitates from the substrate-supported film through a multi-step rinse that was repeated three times. First, we remove soluble contaminants and powder precipitates by isolating substrate-supported films from the reaction mixture and submerging in blank solvent of 5:5:2 volume o-dichlorobenzene:n-butanol:mesitylene (absent monomers), followed by butanol, followed by methanol, where the substrate-supported films are sonicated at low power with minimal to no film damage, and repeated in IPA. All insoluble powder precipitants are then isolated by vacuum filtration while taking care not to allow the powders to dry entirely on the filter paper (35 mg TIIP COF Powder, 60% powder yield). Finally, we activate the substrate-supported TIIP films and TIIP powder materials, separately, by exchanging the final IPA solvent for supercritical $CO_2$, which uses critical point drying to preserve the TIIP structure and avoid crystal collapse through capillary forces from solvent evaporation.

# VII. Structural modeling of TIIP 2DP

Crystal modeling of the 2DP structures was carried out using the Materials Studio (ver.5.0) suite of programs by Accelrys. The initial structures were constructed piecewise starting with a primitive tetragonal (P4) unit cell with lattice parameters determined based on the bonding geometries and lengths of the constituent monomers. The a (and b when relevant) cell parameter was estimated according to the distance between the center of the vertices for each 2DP, and the c parameter was estimated to be 3 Å, which is consistent with the interlayer spacing of vdW stacked crystals. After constructing an elementary prediction, symmetry constraints were removed and the lattice was reassigned as P1. The structures were optimized using the Geometry Optimization routine including energy minimization with cell parameters optimization, using parameters associated with the Universal Force Field method. After the structure had relaxed and new unit cell parameters had been determined, symmetry of the lattice was assigned. The model suggests that TIIP is in a C2/m space group with lattice dimensions: a=43.7 Å, b=45.0 Å, c=3.13 Å. $\alpha$ = 90º, beta = 58º, gamma = 90º corresponding to primitive lattice vectors a1 = a2 = 29.3 Å, c = 3.13 Å and in good agreement with the DFT calculated crystal structure.

Calculation of the simulated powder diffraction patterns and Pawley refinements were performed in the Materials Studio Reflex Plus Module using a Bragg-Brentano geometry. The observed diffraction patterns were subjected to a polynomial background subtraction and then to Pawley refinement wherein peak profiles were refined using the Pseudo-Voigt peak shape function and asymmetry was corrected using the Berar-Baldinozzi function. Surface area calculations were carried out using a Connolly surface calculation using the appropriate parameters for nitrogen as the adsorbed gas. Due to the challenge of predicting the location distribution of mobile side chains, we removed their contribution to the calculated Connolly surface areas.

# VIII. FT-IR, CP-MAS $^{13}C$, and solid state NMR, $N_2$ isotherm, and BET

Fourier transform infrared spectroscopy (FT-IR) exhibits the complete disappearance of an amine and aldehyde feature, accompanied by a corresponding increase in the resonance at the imine stretch, demonstrating that full imine condensation has taken place. We further validate these results on 2DP powder materials generated during film synthesis. $^{13}C$ cross-polarization magic-angle spinning nuclear magnetic resonance spectroscopy shows a lack of aldehyde functionality but a pronounced imine feature. The lack of monomer functionality IR and NMR features indicates that the extent of polymerization in these films is quite high. Nitrogen sorption measurements show typical IV isotherms with a surface area of 1200 $m^2g^{-1}$, which agrees with the predicted surface area and further confirm the high quality of the TIIP film samples.

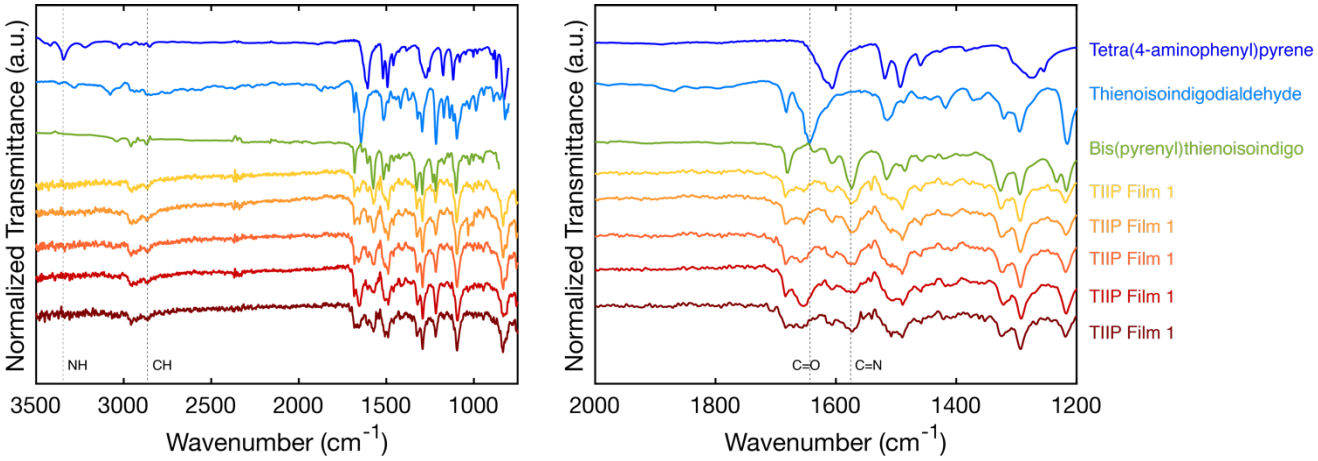


S 13. Fourier-transform infrared spectroscopy (FTIR) spectra of TIIP 2DP films, model compound, and monomer constituents.

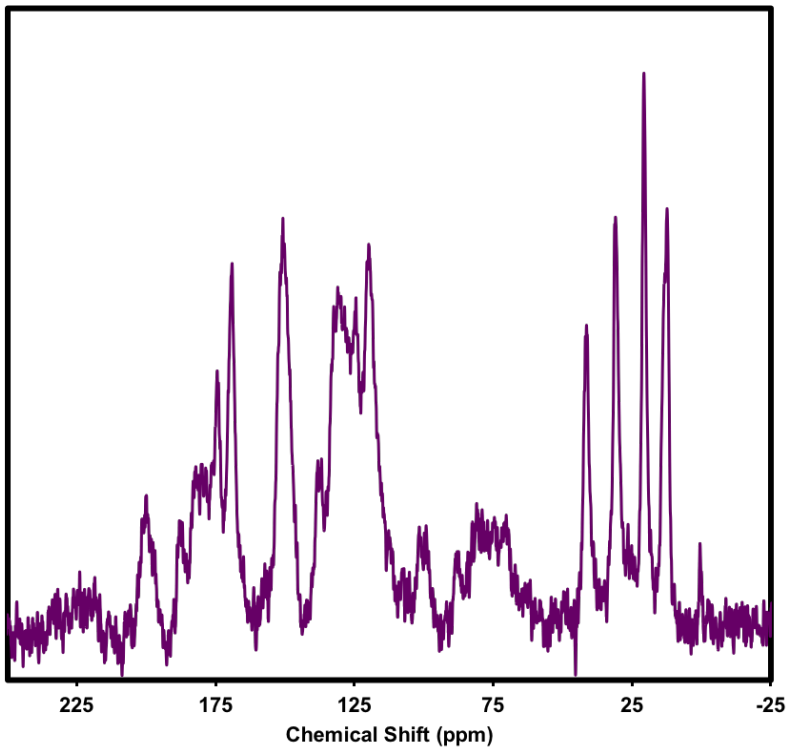


S 14. $^{13}C$ cross-polarization magic-angle spinning nuclear magnetic resonance spectroscopy of TIIP 2D powder.

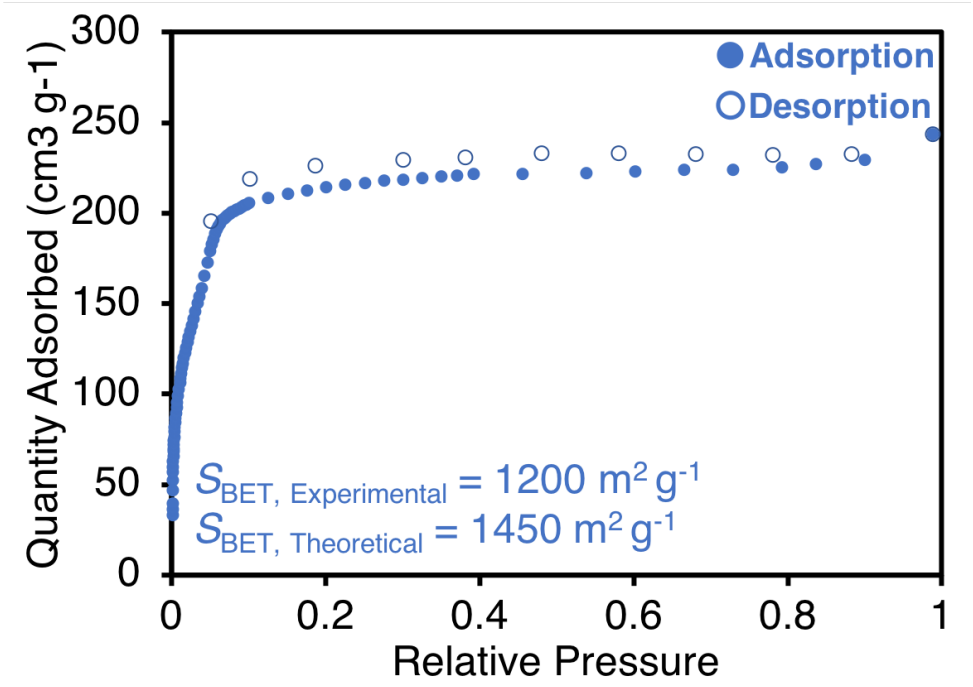


S 15. $N_2$ isotherm of TIIP 2DP powder.

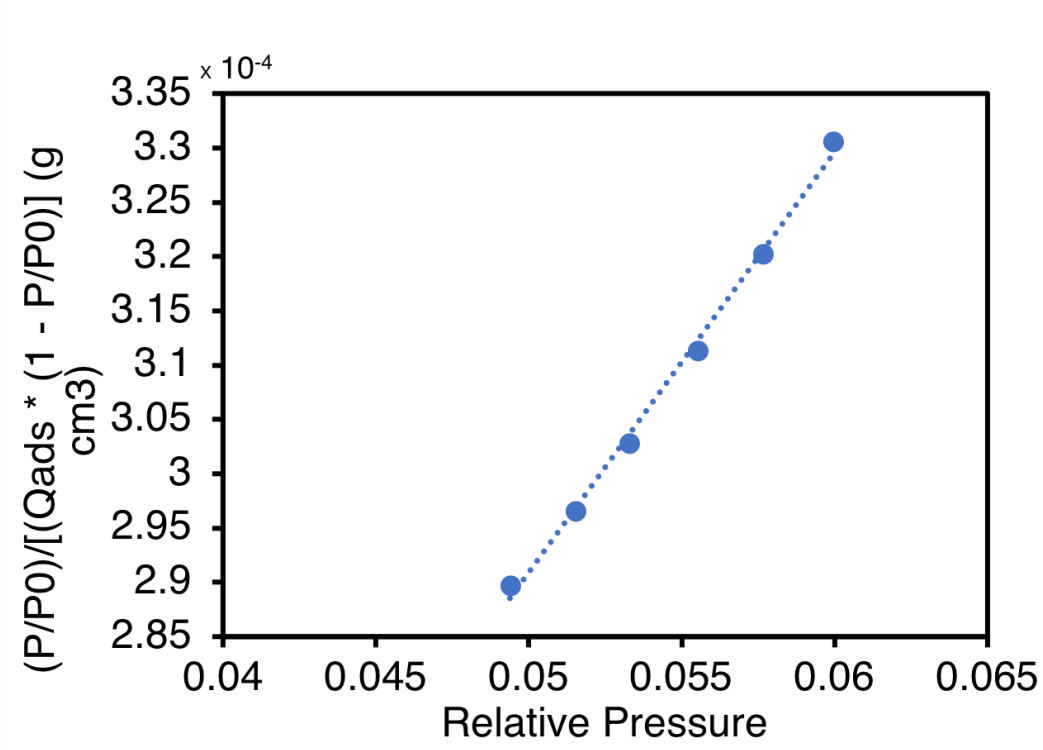


S 16. BET plot of TIIP 2DP powder.

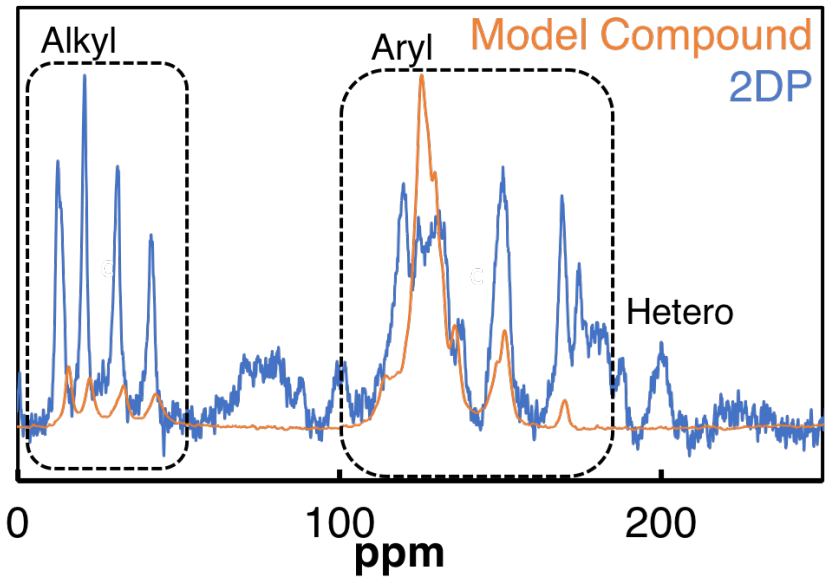


S 17. Solid state NMR of TIIP 2DP powder (blue) and the model compound (orange).

# IX. AFM surface analysis

## Methods

The surface characteristics of the 2DP are measured with atomic force microscopy (AFM). AFM scans were obtained on a Bruker Innova AFM in tapping mode with a drive frequency of ~ 230 kHz, a tapping amplitude of ~ 60 nm, with a setpoint of 3 – 3.6 V.

## Preferential Growth on TMDC

Under optimized solvothermal conditions, TIIP 2DP grows as highly crystalline and oriented films on crystalline substrates. In addition to the high degree of crystalline orientation obtained on TMDCs, TIIP 2DP exhibits preferential growth on the 2D TMDCs, consistent with preferential 2DP growth on graphene[18] and hexagonal boron nitride[19]. The preferential growth of 2DPs has been attributed to a favorable nucleation of 2DP on atomically flat substrates and to energetically favorable van der Waals interactions at the interface[20,21].

## AFM Profilometry

AFM was used to interrogate both height and surface properties of bulk and exfoliated samples. For bulk samples, measurements were taken by making small scratches and delaminated regions that enabled topography profiles from the heterostructure surface to the surrounding 2DP and sapphire substrate, as well as from the surrounding 2DP to the sapphire substrate. The substrate was verified by both control measurements and phase contrast. For ultrathin samples, exfoliation frequently delaminated the 2DP adjacent to the heterostructure (Figure S18 B-C). This enabled measurements to be taken directly from the heterostructure surface to the substrate surface providing a direct measure of heterostructure topography.

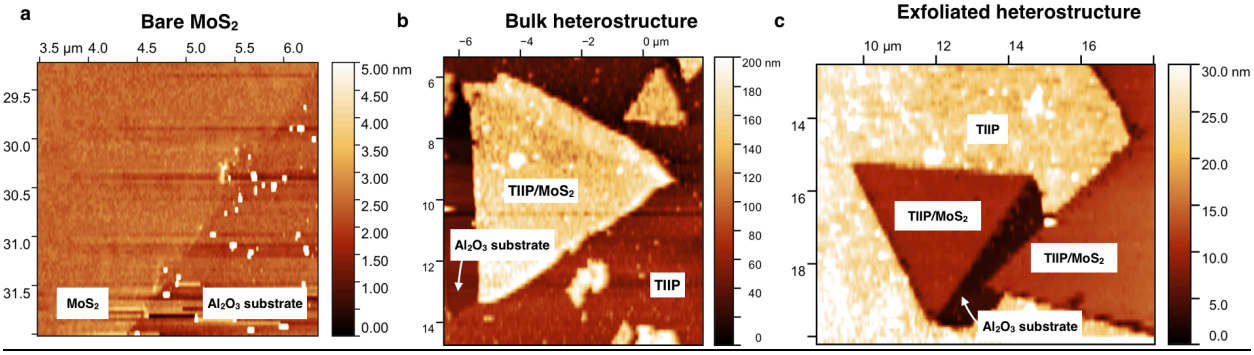


S 18. Atomic force microscopy topographies of a) bare $MoS_2$, b) bulk TIIP/MoS2, and c) exfoliated TIIP/MoS2.

## Surface analysis of exfoliated heterostructures.

AFM of exfoliated heterostructures reveals that ultrathin TIIP films are continuous, uniform, and exhibit low surface roughness across the TIIP/$MoS_2$ flake. The surface roughness is evaluated through both the mean maximum peak-to-valley roughness and the RMS-roughness, respectively. The mean maximum peak-to-valley roughness, $R_{p-p}$, is determined by the difference between the highest peak and the lowest valley sampled across the boxed area in the AFM topographies[22]. The RMS-roughness is the average of the measured height deviations

measured from the mean line across the boxed area, $R_{rms} = \sqrt{\frac{1}{N}\sum_{j=1}^{N} r_j{}^2}$, where for a given line, j, $r_j = z_j - \bar{z}$. Across samples, the mean maximum peak-to-valley roughness ranged from 0.30 nm to 0.57 nm across sampled areas (white boxes, Figure S19). The RMS-roughness spanned 0.12 nm to 0.30 nm (Supplementary Table 1). The sub-nm surface roughness of the ultrathin TIIP/$MoS_2$ across entire $MoS_2$ flakes underscores the high quality of the 2DP films.

| | Flake 1 | Flake 2 |
|---|---|---|
| $MoS_2$ | $R_{p-p}$ = 0.16 nm<br>$R_{rms}$ = 0. 04 nm | |
| TIIP(a) | $R_{p-p}$ = 0.43 nm<br>$R_{rms}$ = 0.23 nm | |
| TIIP(b) | $R_{p-p}$ = 0.34 nm<br>$R_{rms}$ = 0.14 nm | $R_{p-p}$ = 0.42 nm<br>$R_{rms}$ = 0.18 nm |
| TIIP(c) | $R_{p-p}$ = 0.30 nm<br>$R_{rms}$ = 0.12 nm | $R_{p-p}$ = 0.57 nm<br>$R_{rms}$ = 0.25 nm |
| TIIP(d) | $R_{p-p}$ = 0.50 nm<br>$R_{rms}$ = 0.20 nm | $R_{p-p}$ = 0.57 nm<br>$R_{rms}$ = 0.23 nm |
| TIIP(e) | $R_{p-p}$ = 0.52 nm<br>$R_{rms}$ = 0.30 nm | $R_{p-p}$ = 0.42 nm<br>$R_{rms}$ = 0.16 nm |

Supplementary Table 1: Mean maximum peak-to-valley roughness and RMS-roughness of ultrathin TIIP films and of bare $MoS_2$ for comparison.

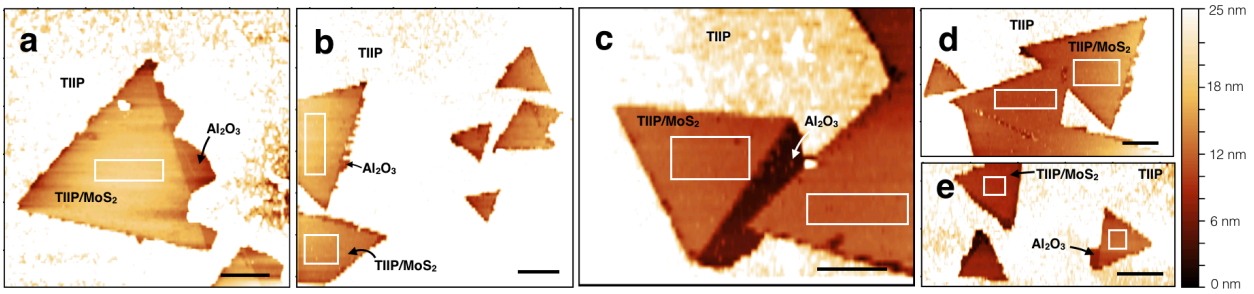


S 19. AFM of additional exfoliated flakes. Scale bar = 2 µm. a) same as Figure 4C in main text. b – e) additional AFM images of exfoliated 2DP films on $MoS_2$. White boxes delineate regions used in surface analyses in the supplementary text.

# X. Transport measurements

We characterized the electrical transport properties of the TIIP 2DP thin films under multiple device configurations. While TIIP is predicted to have a high conductivity among organic lattices, transport measurements are challenging due to the chemical similarity between the 2DP building blocks and the photoresists commonly used to pattern contacts. Instead, we developed methods based on pre-patterning and shadow-mask approaches to measure electrical transport in 2DP films.

Conductivity measurements were performed in a probe station at room temperature using both top and bottom contact geometries. We observe semiconducting behavior in TIIP films in the range of +/− 20 V from both top and bottom contact geometries (Figure S20). The conductivity of the 2DP is extracted from a linear fit to the I-V curve in the low voltage regime (+/− 5 V). For the bottom contacts, we measured five devices which all showed conductivity up to $(2.6 \pm 0.8) \times 10^{-5}$ S/m, reproducibly (Figure S21). In the top contact geometry, conductivity was measured to be $(3.5 \pm 0.7) \times 10^{-5}$ S/m, which is comparable to that measured for the bottom contacts. The conductivities measured here are among the highest reported for undoped COF 2DPs.

**Pre-patterned bottom contacts**

Pre-patterned contacts, which are referred to as bottom contacts, were patterned across a sapphire substrate using photolithography. These pads were patterned using GCA 5x Stepper with S1813 resist. The resist was spun at 3000 rpm and baked at 115 °C for 1 min. After exposure, the sample was developed with AZ 726MIF for 1 min, followed by evaporation of Cr/Au and liftoff. The contacts were deposited as 50 μm by 50 μm square pads, 100 nm in thickness, separated by 2 μm. The TIIP film was grown directly on the pre-patterned substrates by the methods described in Supplementary section SI.VI and in the main text.

**Top contacts**

Top contacts were evaporated using a stencil mask of a thin aluminum wire to form 100 nm thick gold contacts at 4.5 mm square and separated by 20 μm. In addition to validating the pre-patterned contact measurements, an advantage of top contacts is that they can be patterned on samples after-growth, which ensures high-quality films, robust measurements, and permits choice of arbitrary geometries and patterning parameters.

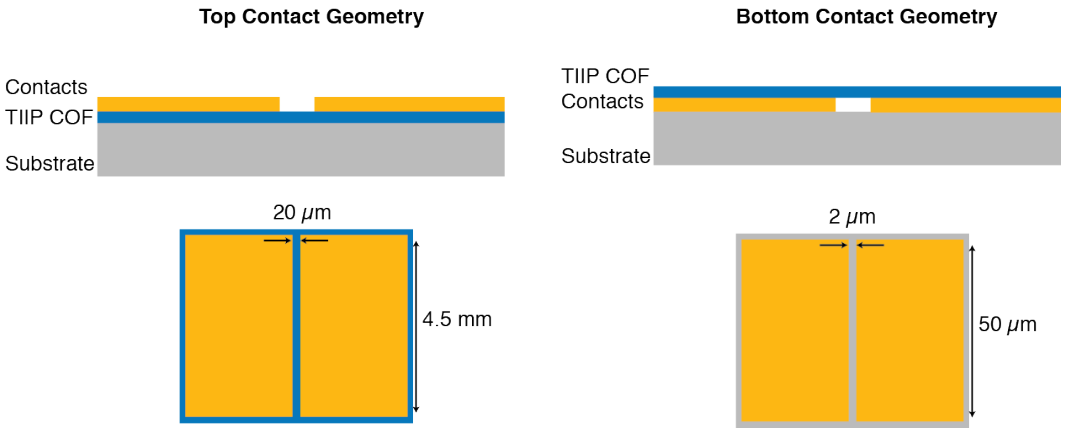


S 20. Schematic of transport measurements of top contact and bottom contact geometry.

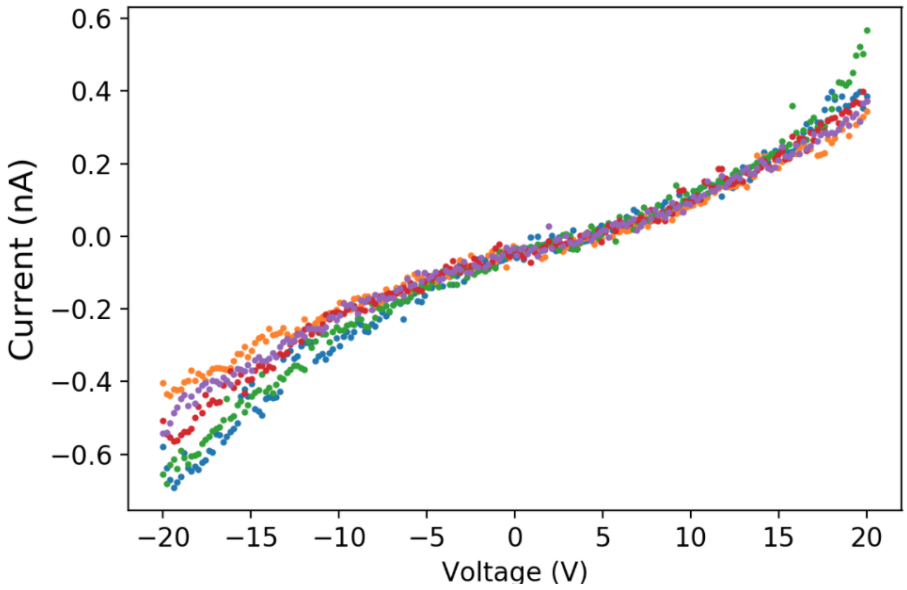


S 21. I-V curves from the bottom contact geometry.

# XI. Exfoliation and transfer of layered 2DP films

We developed dry exfoliation and transfer methods for TIIP 2DP films using pick-up and micromanipulation techniques used in the inorganic 2D material community[23,24]. TIIP 2DP is formed of covalently bonded two-dimensional lattices that are layered through van der Waals bonding. While exfoliation of 2DPs has been demonstrated through chemical exfoliation of powders, dry-exfoliation methods that are amenable to large-area and crystalline film growth are necessary to enable the formation of functional heterostructures and device platforms.

The experimental setup comprises of an optical microscope paired with long working-distance objectives (Mitutoyo 5X and 20X) and a three-axis micrometer stage, which permits accurate positioning of the polyethylene terephthalate (PET) stamp (Figure S22). While this approach is general, in this study, the bulk sample comprised a 1 mm x 3 mm double-sided polished $Al_2O_3$ chip containing single crystal CVD-grown $MoS_2$ flakes (edge length ~ 1-8 μm) covered by solvothermally grown TIIP 2DP film. The bulk TIIP film was prepared as described in the Supplementary section SI.VI on film synthesis. The exfoliated area was < 1 $mm^2$ area and used a fresh PET stamp prepared as described below.

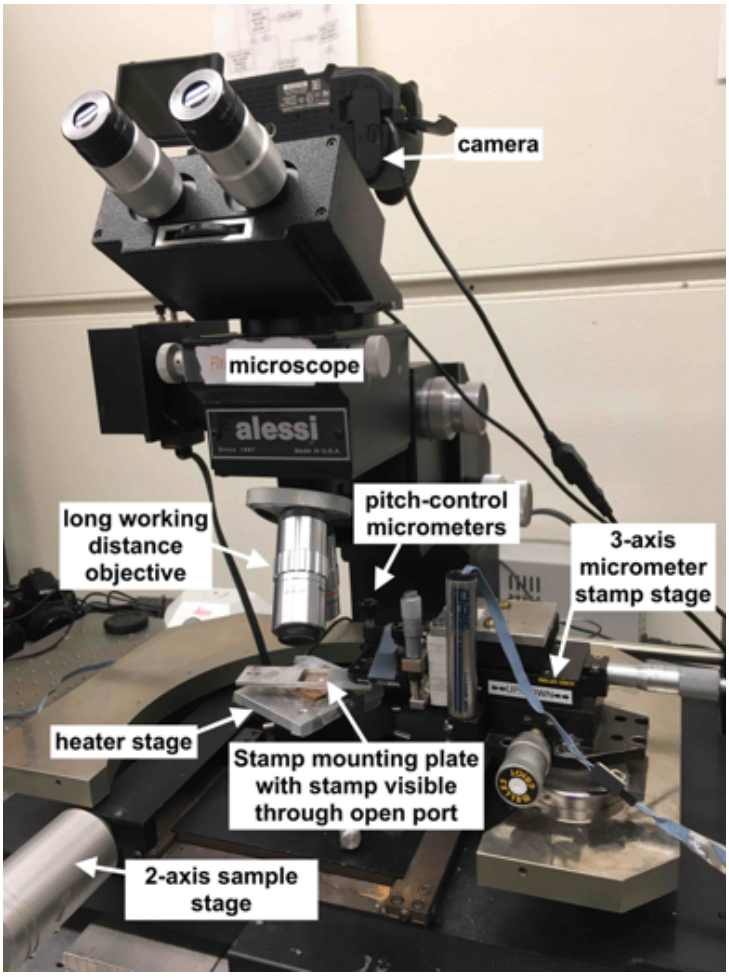


S 22. Exfoliation set-up: coupled 3-axis micromanipulation stage to a 3-axis sample stage permits in situ microscopy of the stamp and sample.

***Part I: Making the stamp***

In preparing the polymer pick-up stamp, start with a clean and flat stamp surface. Using a sharp blade or scissors, the PET is cut into a ~5 mm x 5 mm square and the protective plastic covering is removed from the rough side of the PET. This side is affixed to a clean glass slide ("mounting slide") with permanent double-sided tape and a second glass slide is firmly pressed down on the PET/tape/mounting slide stack to ensure good contact with the tape and mounting slide. The protective plastic covering is then removed from the smooth side. If the contact between the stamp, adhesive, and mounting slide is sufficient, the stack will be transparent. Using a clean sharp razor blade, the PET edges are then cut in one smooth motion to each of the four sides until the edges of the PET appear, under a microscope, sharp and single-leveled with no visible bubbles or debris. The stamp will be ~ 1-2 mm-square at this time.

***Part II: Cleaning and flattening the stamp***

The mounting slide is screwed to the stamp mounting plate with the stamp face-down towards the sample stage of the microscope. A clean $Si/SiO_2$ chip is placed on the sample chuck and affixed by vacuum or adhesive. The temperature of the chuck is then increased to ~ 45 C. The stamp is centered in the field of view of the microscope such that the microscope can be focused, through the stamp, on the chip surface. The stamp and sample chuck will now be within the same field of view as the stamp is lowered to the image plane at the substrate. The stamp is lowered until one edge makes contact with the clean $Si/SiO_2$ substrate. The incident corner will produce an interference pattern. The tighter the interference pattern, the steeper the incident angle of the stamp; the larger the interference pattern, the closer the stamp surface is to parallel with the substrate. The incident angle is adjusted using pitch-control micrometers until the stamp lands on the substrate nearly simultaneously, producing a roughly symmetric interference pattern from the center of the stamp. Flatten the stamp: The stamp is lowered parallel to the substrate until it comes into contact with a clean section of the substrate. The chuck is heated to 65-70 C at which point the stamp will form a complete contact with the substrate. The temperature is lowered to 25 C for 3 minutes before the slab mounting plate is lifted up.

***Part III: Exfoliation***

Using the pitch control, the stamp is tilted by <1 deg such that only one side of the stamp touches the substrate first, but does so at a shallow angle. This is the "leading stamp edge". The stamp is carefully raised and the substrate is replaced by the chip containing the bulk heterostructure on the sample chuck. Through the long working distance objective, the region of the chip containing bulk heterostructure is identified. This region should be free of debris. Using the sample translation stage, this region is aligned directly below the stamp. The sample stage is oriented such that the leading edge of the stamp will make contact with the substrate adjacent to the heterostructures of interest. The stamp is manually lowered until the leading edge makes initial contact with the sample chip. The motorized stage is used to lower the stamp at a rate of ~1.0 μm/s. The stamp continues to be lowered until it makes complete or nearly complete contact. After sitting for 1 minute, the temperature is increased to 35-40 C for 5 minutes. The temperature is then lowered to 25 C for 2 minutes before the stamp is continuously raised by the motorized stage. With successful lamination, as the stamp lifts, multiple layers of TIIP will remain on the stamp and few-layered 2DP/TMDC heterostructures remain on the substrate. Due to the few-μm area of CVD $MoS_2$ flakes

and their relative density, a single exfoliation procedure produced several dozen exfoliated flakes. The thickness of the exfoliated flakes varied from ~2 nm - 10 nm across the exfoliated area, roughly proportional to the distance from the leading stamp edge: flakes closest to the leading edge were thinnest and progressively increased in thickness away from the edge. A single area was never exfoliated more than once and a single stamp was never reused. Measurements of exfoliated heterostructures reflect the freshly cleaved surface.

***Part IV: Transfer***

The TIIP film adhered to the stamp can be immediately transferred to other experimental platforms such as transport stages, contacts, or TEM grids for further measurements. To transfer the 2DP film, the sample chip is replaced with a clean substrate (e.g. $Si/SiO_2$, fused silica, or TEM grid). The PET stamp containing bulk film exfoliated from the heterostructure is immediately stamped onto this clean substrate using the motorized stage and viewed through the microscope. For TEM transfer, the TEM grid is placed on a clean substrate and aligned via the microscope viewfinder. Once stamped, the substrate/2DP/PET stack is heated to 80 C and then lowered to 25 C. The grid/2DP/PET stack is then placed on one edge in dichloromethane at room temperature until the PET stamp detaches from the 2DP/substrate stack. This stack is removed and placed in fresh dichloromethane at room temperature for 12 hours. The 2DP/substrate is rinsed in IPA at room temperature. The TIIP films are activated by exchanging the final IPA solvent for supercritical $CO_2$, to preserve the TIIP structure and avoid crystal collapse through capillary forces from solvent evaporation. Though supercritical $CO_2$ activation is necessary to retain the crystallinity, films transferred to TEM grids via wet-transfer nonetheless exhibit a decrease of the lattice constant relative to the un-transferred lattice, which retain the as-synthesized periodicity of 2.9 nm verified in both TEM and GIWAXS. This is likely due to small modifications of the pore structure due to solvent evaporation during the dissolution of PET from the film surface. These results are consistent with the formation of the high quality TIIP 2DP and underscore the importance of the dry manipulation techniques presented here and the development of all-dry techniques for the range of manipulations necessary for future device applications.

# XII. Transmission electron microscopy

TEM of the TIIP samples were performed using a JEOL (JEOL USA, Inc., Peabody, MA) ARM300F GrandARM TEM operating at 300 keV equipped with a Gatan (Gatan, Inc., Pleasanton, CA) K3-IS "direct electron" detector (FEG Emission: 15 μA, spot size 5, 150 μm CL aperture). The ARM300F was aligned for low-dose imaging, measuring the dose rate on the K3 detector through vacuum (no grid inserted). The dose rate used was 40-133 $e^- Å^{-2} s^{-1}$ (5760 × 4092 pixels, binning 2), with image exposure times of 0.1 s - 1 s (11-43 $e^- Å^{-2}$ cumulative dose per image). Additional data are shown below. Data presented in the main text (Figure 2D) and Figure S23 was taken using a dose rate of 40.3 $e^- Å^{-2} s^{-1}$ and a cumulative dose of 19.5 $e^- Å^{-2}$. The bandpass filtered image (S23.F) was obtained by applying a mask to the FFT (S23.D-E) of the cropped HR-TEM image as outlined below.

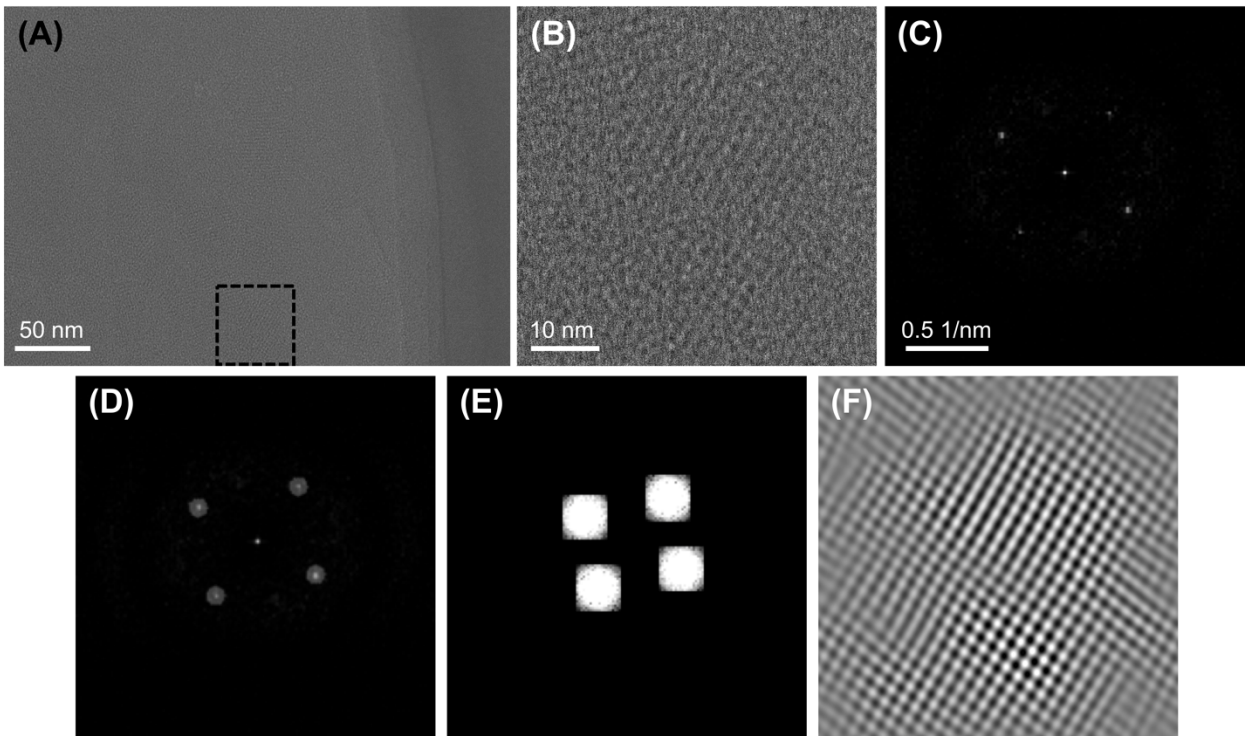


S 23. HR-TEM analysis of data presented in the main text (Figure 2D). a) Full HR-TEM image of TIIP film b) Cropped HR-TEM image of boxed region in (a). c) FFT pattern of (b) cropped at the predominant lattice spacings. d) FFT pattern with masks placed over the FFT spots. e) Image produced after the mask is applied to the FFT pattern, eliminating the signal outside of the masked region and smoothing the edges by 5 pixels. f) Inverse FFT of (e) produces filtered real space image of (b).

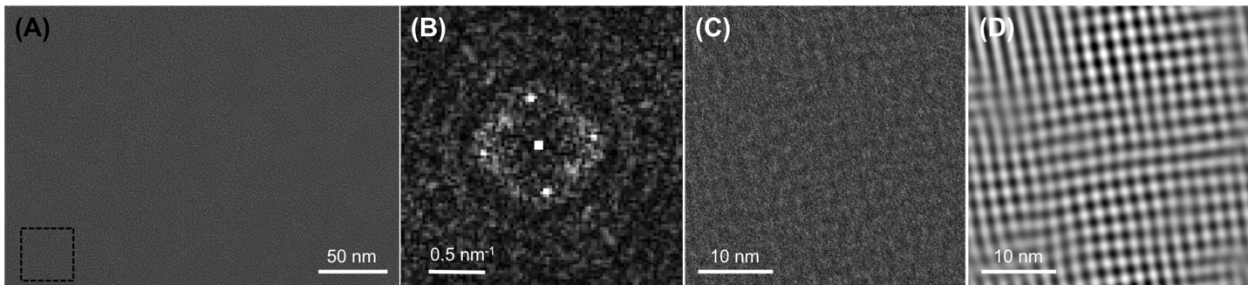


S 24. a) HR-TEM image of TIIP on $MoS_2$. b) FFT of boxed region in (a). c) Zoomed-in image of boxed region in (a). d) Bandpass filtered image of boxed region in (a). Dose rate/Cumulative Dose: 133.17 $e^- Å^{-2} s^{-1}$ / 13.83 $e^- Å^{-2}$.

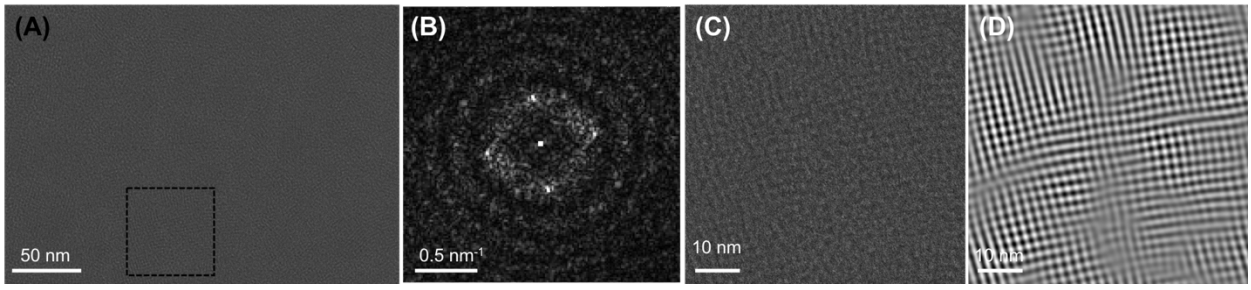


S 25. a) HR-TEM image of TIIP on $MoS_2$. b) FFT of boxed region in (a). c) Zoomed-in image of boxed region in (a). d) Bandpass filtered image of boxed region in (a). Dose rate/Cumulative Dose: 132.87 $e^- Å^{-2} s^{-1}$ / 13.80 $e^- Å^{-2}$.

# XIII. Absorption of $MoS_2$ and TIIP/ $MoS_2$ heterostructures

**Reflection contrast of $MoS_2$**

Reflection contrast measurements were obtained under vacuum at 77 K on a home-built reflection microscopy setup using a pulsed supercontinuum laser source and a 50X objective as described in the Methods section. The reference spectrum, $R_0$, was taken on the sapphire substrate next to the single crystal CVD $MoS_2$ sample. The normalized difference signal ($R$-$R_0/R_0$) is directly proportional to the linear absorption from thin layers on sapphire.

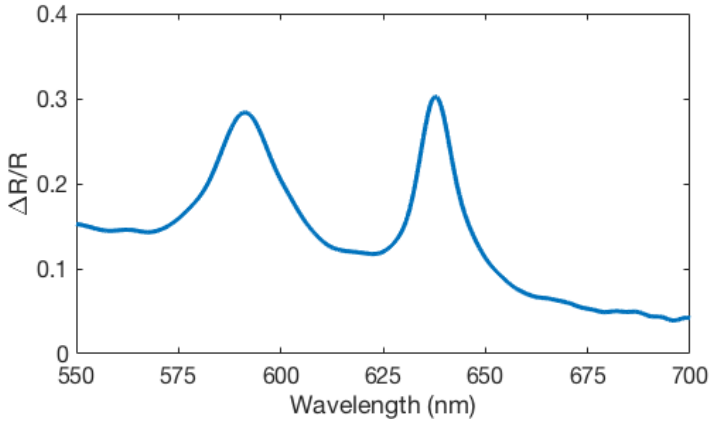


S 26. Reflection contrast of monolayer CVD $MoS_2$ at 77 K exhibiting the A and B exciton resonances of $MoS_2$ at 1.9 eV and 2.1 eV, respectively.

**Transmission contrast of bulk TIIP/$MoS_2$ heterostructure**

Transmission contrast ($T$-$T_0/T_0$) measurements on the heterostructure were obtained at room temperature under ambient conditions on a home-built microscopy setup. The references spectrum, $T_0$, was taken on the sapphire substrate next to the heterostructure and next to the bare $MoS_2$ respectively. The bulk TIIP/$MoS_2$ heterostructure exhibits the broad absorption of the TIIP 2DP and the two absorption resonances corresponding to the $MoS_2$ A- and B-excitons.

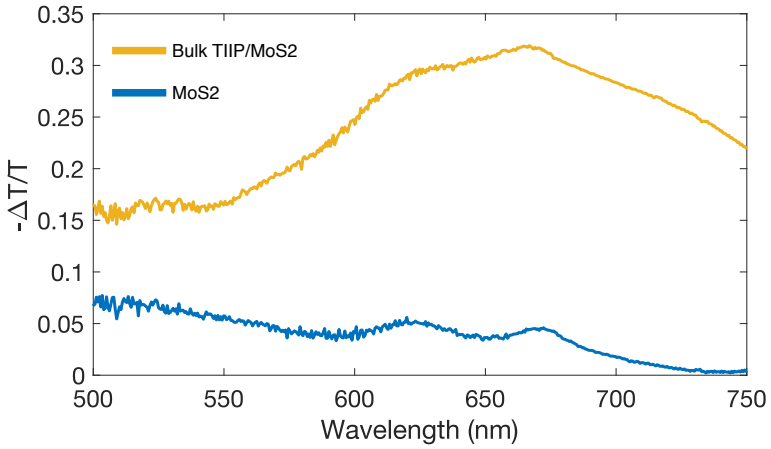


S 27. Room temperature transmission contrast of bulk TIIP/MoS2 (yellow) and monolayer CVD $MoS_2$ (blue) for reference.

# XIV. GIWAXS of TIIP on TMDCs

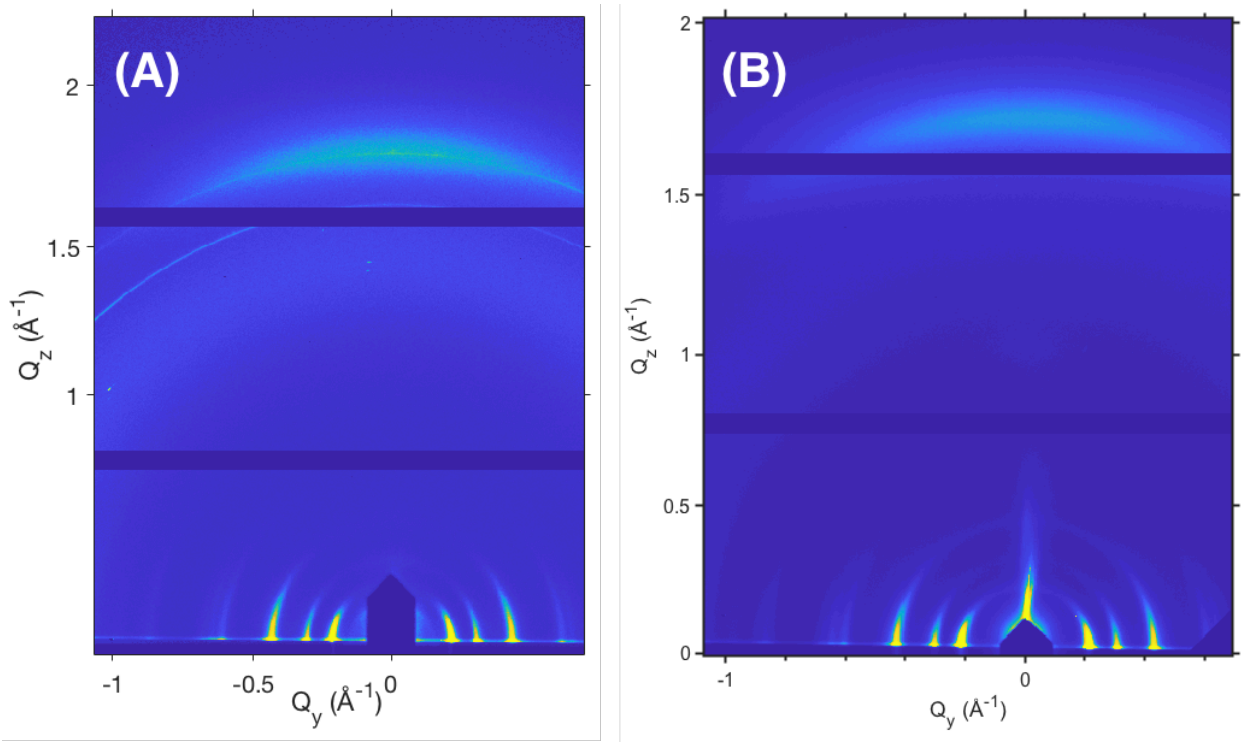


S 28. GIWAXS of highly crystalline 2DP TIIP on monolayer TMDCs. a) GIWAXS scattering from TIIP on monolayer $WSe_2$. b) GIWAXS scattering from TIIP on monolayer $MoSe_2$.

## Supplemental References


(1) Cheng, Y. J.; Yang, S. H.; Hsu, C. S. Synthesis of Conjugated Polymers for Organic Solar Cell Applications. *Chem. Rev.* **2009**, *109* (11), 5868–5923. https://doi.org/10.1021/cr900182s.

(2) Dutta, G. K.; Han, A. R.; Lee, J.; Kim, Y.; Oh, J. H.; Yang, C. Visible-near Infrared Absorbing Polymers Containing Thienoisoindigo and Electron-Rich Units for Organic Transistors with Tunable Polarity. *Adv. Funct. Mater.* **2013**, *23* (42), 5317–5325. https://doi.org/10.1002/adfm.201300536.

(3) Kim, G.; Kang, S.; Dutta, G. K.; Han, Y.; Shin, T. J.; Noh, Y.; Yang, C. A Thienoisoindigo-Naphthalene Polymer with Ultrahigh Mobility of 14.4 Cm 2 /V · s That Substantially Exceeds Benchmark Values for Amorphous Silicon Semiconductors. **2014**.

(4) Wan, S.; Guo, J.; Kim, J.; Ihee, H.; Jiang, D. A Belt-Shaped, Blue Luminescent, and Semiconducting Covalent Organic Framework. *Angew. Chemie Int. Ed.* **2008**, *47* (46), 8826–8830. https://doi.org/10.1002/anie.200803826.

(5) Gao, Q.; Li, X.; Ning, G. H.; Leng, K.; Tian, B.; Liu, C.; Tang, W.; Xu, H. Sen; Loh, K. P. Highly Photoluminescent Two-Dimensional Imine-Based Covalent Organic Frameworks for Chemical Sensing. *Chem. Commun.* **2018**, *54* (19), 2349–2352. https://doi.org/10.1039/c7cc09866a.

(6) Bessinger, D.; Ascherl, L.; Auras, F.; Bein, T. Spectrally Switchable Photodetection with Near-Infrared-Absorbing Covalent Organic Frameworks. *J. Am. Chem. Soc.* **2017**, *139* (34), 12035–12042. https://doi.org/10.1021/jacs.7b06599.

(7) Jiang, Z. GIXSGUI: A MATLAB Toolbox for Grazing-Incidence X-Ray Scattering Data Visualization and Reduction, and Indexing of Buried Three-Dimensional Periodic Nanostructured Films. *J. Appl. Crystallogr.* **2015**, *48* (3), 917–926. https://doi.org/10.1107/S1600576715004434.

(8) Ilavsky, J. Nika package https://usaxs.xray.aps.anl.gov/software/nika.

(9) Hong, X.; Kim, J.; Shi, S. F.; Zhang, Y.; Jin, C.; Sun, Y.; Tongay, S.; Wu, J.; Zhang, Y.; Wang, F. Ultrafast Charge Transfer in Atomically Thin MoS2/WS2 Heterostructures. *Nat. Nanotechnol.* **2014**, *9* (9), 682–686. https://doi.org/10.1038/nnano.2014.167.

(10) Matsumoto, M.; Dasari, R. R.; Ji, W.; Feriante, C. H.; Parker, T. C.; Marder, S. R.; Dichtel, W. R. Rapid, Low Temperature Formation of Imine-Linked Covalent Organic Frameworks Catalyzed by Metal Triflates. *J. Am. Chem. Soc.* **2017**, *139* (14), 4999–5002. https://doi.org/10.1021/jacs.7b01240.

(11) Auras, F.; Ascherl, L.; Hakimioun, A. H.; Margraf, J. T.; Hanusch, F. C.; Reuter, S.; Bessinger, D.; Döblinger, M.; Hettstedt, C.; Karaghiosoff, K.; Herbert, S.; Knochel, P.; Clark, T.; Bein, T. Synchronized Offset Stacking: A Concept for Growing Large-Domain and Highly Crystalline 2D Covalent Organic Frameworks. *J. Am. Chem. Soc.* **2016**, *138* (51), 16703–16710. https://doi.org/10.1021/jacs.6b09787.

(12) Calik, M.; Sick, T.; Dogru, M.; Döblinger, M.; Datz, S.; Budde, H.; Hartschuh, A.; Auras, F.; Bein, T. From Highly Crystalline to Outer Surface-Functionalized Covalent Organic Frameworks – A Modulation Approach. *J. Am. Chem. Soc.* **2015**, jacs.5b10708. https://doi.org/10.1021/jacs.5b10708.

(13) Castano, I.; Evans, A. M.; Li, H.; Vitaku, E.; Strauss, M. J.; Brédas, J. L.; Gianneschi, N. C.; Dichtel, W. R. Chemical Control over Nucleation and Anisotropic Growth of Two-Dimensional Covalent Organic Frameworks. *ACS Cent. Sci.* **2019**, *5* (11), 1892–1899.

https://doi.org/10.1021/acscentsci.9b00944.
(14) Smith, B. J.; Dichtel, W. R. Mechanistic Studies of Two-Dimensional Covalent Organic Frameworks Rapidly Polymerized from Initially Homogenous Conditions. *J. Am. Chem. Soc.* **2014**, *136* (24), 8783–8789. https://doi.org/10.1021/ja5037868.
(15) Li, H.; Evans, A. M.; Castano, I.; Strauss, M. J.; Dichtel, W. R.; Bredas, J. L. Nucleation-Elongation Dynamics of Two-Dimensional Covalent Organic Frameworks. *J. Am. Chem. Soc.* **2020**, *142* (3), 1367–1374. https://doi.org/10.1021/jacs.9b10869.
(16) Li, H.; Chavez, A. D.; Li, H.; Li, H.; Dichtel, W. R.; Bredas, J. L. Nucleation and Growth of Covalent Organic Frameworks from Solution: The Example of COF-5. *J. Am. Chem. Soc.* **2017**, *139* (45), 16310–16318. https://doi.org/10.1021/jacs.7b09169.
(17) Nguyen, V.; Grünwald, M. Microscopic Origins of Poor Crystallinity in the Synthesis of Covalent Organic Framework COF-5. *J. Am. Chem. Soc.* **2018**, *140* (9), 3306–3311. https://doi.org/10.1021/jacs.7b12529.
(18) Colson, J. W.; Woll, A. R.; Mukherjee, A.; Levendorf, M. P.; Spitler, E. L.; Shields, V. B.; Spencer, M. G.; Park, J.; Dichtel, W. R. Oriented 2D Covalent on Single-Layer Graphene. **2011**, No. April, 228–232.
(19) Sun, B.; Li, J.; Dong, W.; Wu, M.; Wang, D. Selective Growth of Covalent Organic Framework Ultrathin Films on Hexagonal Boron Nitride. *J. Phys. Chem. C* **2016**, *120* (27), 14706–14711. https://doi.org/10.1021/acs.jpcc.6b04410.
(20) Liu, X. H.; Guan, C. Z.; Wang, D.; Wan, L. J. Graphene-like Single-Layered Covalent Organic Frameworks: Synthesis Strategies and Application Prospects. *Adv. Mater.* **2014**, *26* (40), 6912–6920. https://doi.org/10.1002/adma.201305317.
(21) Kudernac, T.; Lei, S.; Elemans, J. A. A. W.; De Feyter, S. Two-Dimensional Supramolecular Self-Assembly: Nanoporous Networks on Surfaces. *Chem. Soc. Rev.* **2009**, *38* (2), 402–421. https://doi.org/10.1039/b708902n.
(22) Gwyddion user guide http://gwyddion.net/documentation/user-guide-en/ (accessed Jul 21, 2020).
(23) Wang, L.; Meric, I.; Huang, P. Y.; Gao, Q.; Gao, Y.; Tran, H.; Taniguchi, T.; Watanabe, K.; Campos, L. M.; Muller, D. A.; Guo, J.; Kim, P.; Hone, J.; Shepard, K. L.; Dean, C. R. One-Dimensional Electrical Contact to a Two-Dimensional Material. *Science (80-. ).* **2013**, *342* (6158), 614–617. https://doi.org/10.1126/science.1244358.
(24) Novoselov, K. S.; Mishchenko, A.; Carvalho, A.; Castro Neto, A. H. 2D Materials and van Der Waals Heterostructures. *Science*. American Association for the Advancement of Science July 29, 2016. https://doi.org/10.1126/science.aac9439.